Co-seismic and postseismic deformation, field observations and fault model of the October 30, 2020 Mw=7.0 Samos earthquake, Aegean Sea

Athanassios Ganas, Panagiotis Elias, Pierre Briole, Sotiris Valkaniotis, Javier Escartin, Varvara Tsironi, Ilektra Karasante, Chrysanthi Kosma

Co-seismic and postseismic deformation, field observations and fault model of the October 30, 2020 M_w=7.0 Samos earthquake, Aegean Sea.

Athanassios Ganas[1], Panagiotis Elias[2], Pierre Briole[3], Sotiris Valkaniotis[4], Javier Escartin[3], Varvara Tsironi[1,5,] Ilektra Karasante[1] and Chrysanthi Kosma[1].

[1]National Observatory of Athens, Institute of Geodynamics, Lofos Nymfon, Thission, 11810 Athens, Greece; aganas@noa.gr ; vtsironi@noa.gr ; hlekara@hotmail.com ; chrysanthi.kosma.varela@gmail.com

[2]National Observatory of Athens, Institute of Astronomy, Astrophysics, Space Applications and Remote Sensing, Vas. Pavlou & I. Metaxa, GR-15 236 Penteli, Greece ; pelias@noa.gr

[3]Ecole Normale Supérieure de Paris, PSL Research University, Laboratoire de Géologie - UMR CNRS 8538, 24 rue Lhomond, 75005 Paris – France briole@ens.fr ; escartin@geologie.ens.fr

[4]Department of Civil Engineering, Democritus University of Thrace, 67100 Xanthi, Greece valkaniotis@yahoo.com

[5]Department of Geology, University of Patras, 26504 Rio, Greece

* Correspondence: aganas@noa.gr Tel.: +30 210 3490186 (A.G.)

Abstract

On 30 October 2020 a large M_w = 7.0 earthquake occurred north of the island of Samos, Greece. Here we present the characteristics of the seismic fault (location, geometry, geodetic moment) as inferred from the processing of geodetic data (InSAR and GNSS). We use the InSAR displacement data from Sentinel-1 interferograms (ascending orbit 29 and descending 36) and the GNSS offsets from fourteen (14) stations in Greece and Turkey to invert for the fault parameters. Our inversion modeling indicates the activation of a normal fault offshore Samos with a length of 40 km, width of 15 km, average slip of 1.7 m, a moderate dip-angle (37°) and with a dip-direction towards North. The inferred fault is located immediately north of, and adjacent to Samos, with the top of the slip ~ 0.6 km below surface, and ~1 km off-shore at its closest to the island. Near the fault the earthquake caused the permanent uplift of the island up to 10 cm with the exception of a coastal strip along the NE part of the northern shore that subsided 2-6 cm. The co-seismic horizontal motion of GNSS station SAMO was 35.6 cm towards south and 3 cm towards west. A postseismic signal (22-33% of the co-seismic on the vertical component) was observed at GNSS stations SAMO and SAMU, with a time constant of 30 days. The effects of the earthquake included liquefaction, rock falls, rock slides, road cracks and deep-seated

landslides, all due to the strong ground motion and associated down-slope mobilization of soil cover and loose sediments.

K**eywords**: earthquake, InSAR, GNSS, liquefaction, uplift, Samos, Aegean

1. Introduction - Tectonic Setting

The Samos island is located in the eastern Aegean Sea, a well-known extensional terrain, as it is found on the back-arc area behind the Hellenic subduction (Fig. 1; McKenzie, 1978; Angelier, 1979; Taymaz et al. 1991; Ganas and Parsons, 2009; Meng et al. 2021). The plate kinematics are determined by the ongoing northward subduction of the African slab under the Aegean continental lithosphere and the synchronous, westwards motion of the Anatolian microplate. The GPS velocity field, with respect to Eurasia (fixed reference), is characterised by a counter-clockwise rotation of the continental plate, with increasing GPS velocities from eastern Anatolia towards the Hellenic trench (McClusky et al. 2000; Reilinger et al. 2010; Briole et al. 2021). Within this setting the central Aegean block (including Samos) moves almost uniformly southwest (S24°W) at an average velocity of ~30 mm/yr (w.r.t to Europe; Briole et al. 2021; revising the 33 mm/yr value of Ganas and Parsons, 2009; Vernant et al. 2014). This velocity plateau marks the end of the significant increase in N-S extension of the whole Aegean as observed from North to South (Briole et al. 2021, their Fig. S29; see also McClusky et al. 2000; D'Agostino et al. 2020). Crustal extension is accommodated by seismic slip along normal-slip and strike-slip active faults, that are scattered throughout the north and central Aegean and western Anatolia (Mascle and Martin, 1990; Taymaz et al. 1991; Ganas et al. 2005; Chatzipetros et al. 2013; Tan et al. 2014; Yolsal-Çevikbilen et al. 2014; Melis et al. 2020). The last seismic activity in the broader Samos area was the October 2005 seismic sequence in Seferihisar – Sigacik (Benetatos et al. 2006; Fig. 1) in the Turkish coastal area (North of Samos), involving strike-slip ruptures with moment magnitudes in the range 5.4-5.8.

The geology of Samos comprises metamorphic and carbonate rocks of Mesozoic and early Cenozoic age that bound two Neogene sedimentary basins (mostly composed of marls and sandstone formations; Theodoropoulos, 1979). The metamorphic complex of Samos is composed mainly of marbles and phyllites, serpentinites, blueschists and greenschists (Okrusch et al. 1984). The active tectonics is dominated by extensional kinematics along numerous faults (Boronkay and Doutsos, 1994; Ring et al. 1999) with fault-slip data indicating nearly N-S extension (Boronkay and Doutsos, 1994). A major, north-dipping normal fault occurs just north of the island (Fig. 1) and it tilted Samos Island to the south (Ring et al. 1999; Chatzipetros et al. 2013; Nomikou et al. 2021). Geological evidence (marine biogenic notches now found above mean sea level) suggests that a large part of

the northwestern coastline has been uplifted due to a combination of regional geodynamics and earthquake activity (Stiros et al. 2000; Evelpidou et al. 2021).

As the 30 October 2020 epicentre is located offshore Samos (Fig. 1) we investigated the bathymetric features (submarine scarps, ridges etc.) and other geophysical evidence for active faulting. The grids publicly available (gmrt https://www.gmrt.org/; emodnet https://emodnet.eu) show that overall depths of the basin north of Samos mark a deepening from ~500 m to 1000 m towards the west. Early seismic profiles in this area of the Aegean are limited to the Ikaria area, and reveal a half-graben offshore structure (Mascle and Martin, 1990). Immediately following the Samos earthquake, a bathymetry survey of the area north of Samos and around the earthquake epicentre revealed ~E-W seafloor structures consistent with the surface expression of a normal fault scarp, showing seafloor slopes of 30-50°, and bounding the Samos Basin that is interpreted as a half-graben (Nomikou et al., 2021). These data are consistent with a normal faulting event nucleating in the prolongation towards the north of this fault's trace (Nomikou et al., 2021), and also reveal numerous mass wasting scarps and deposits throughout, that may be linked to the long-term activity of this fault system.Around Samos – Kuşadası (Fig. 1) Tan et al (2014) showed that the seismicity is heterogeneously distributed including an activity offshore Samos in the vicinity of the epicentre of the 2020 Samos earthquake, and that there is microseismic activity onshore Samos as well as onshore activity in the Kuşadası area.

In terms of finite strain, the amount of crustal extension between Samos and the Menderes region of western Anatolia (including the broader Izmir area) ranges from 5.3-7.4 mm/yr according to Vernant et al. (2014; with 0.8-1.0 mm/yr uncertainty) based on GNSS data modeling. New GNSS data provide an extension rate of 6.2 ± 0.7 mm/yr between eastern Samos and Izmir (Fig. 1; Briole et al. 2021). A component of left-lateral slip was also proposed by Vernant et al. (2014; 4.8-5.0 mm/yr) along with their proposed WNW-ESE crustal boundary offshore Samos.

Previous seismicity around Samos includes a cluster of poorly-located M=6.0+ events in 1904 (Ambraseys, 2001; Fig. 1). A M_S=6.1 (surface magnitude) event occurred on 11 August 1904 (this event is reported as M=6.8 in the online catalog of AUTH's seismological laboratory) south of Samos, followed by a M_S=6.0 event on 18 August 1904; a third event with M_S=6.0 occurred on 10 October 1904. All those events caused severe damage to Samos and settlements along the Turkish coast. Eight (8) M≥6.0 size events are reported by Tan et al. (2014) to have affected Samos during the 19th century. A M=7.0 event occurred in 1955 to the southeast of Samos, probably on the normal fault bounding the northern side of the Büyük Menderes graben (Fig. 1). During October 2005 three moderate events (5.4≤M≤5.8) occurred west of Seferihisar, Turkey (Fig. 1) about 40 km north of Samos (Benetatos et al. 2006; Papadopoulos et al. 2006).

In this paper we use geodetic observations (GNSS and InSAR) to model the seismic fault (sections 3, 4 and 5). The fringes in the interferograms onshore Samos show a pattern that

supports more the north-dipping fault plane. Even if the InSAR data cover only a portion of the deformation field, it allows us to distinguish between the two patterns (north-dip vs. south dip) in terms of gradient, density, curvature and the concentration patches of the fringes. We also present field observations (section 6) including liquefaction phenomena and InSAR data suggesting massive gravitational movements and discuss our findings in terms of footwall deformation patterns (section 7). We show that both InSAR and GNSS data provided evidence for co-seismic and postseismic deformation (uplift) of northern Samos. We finally discuss the significance of our findings for the active tectonics and strain in this part of the Aegean.

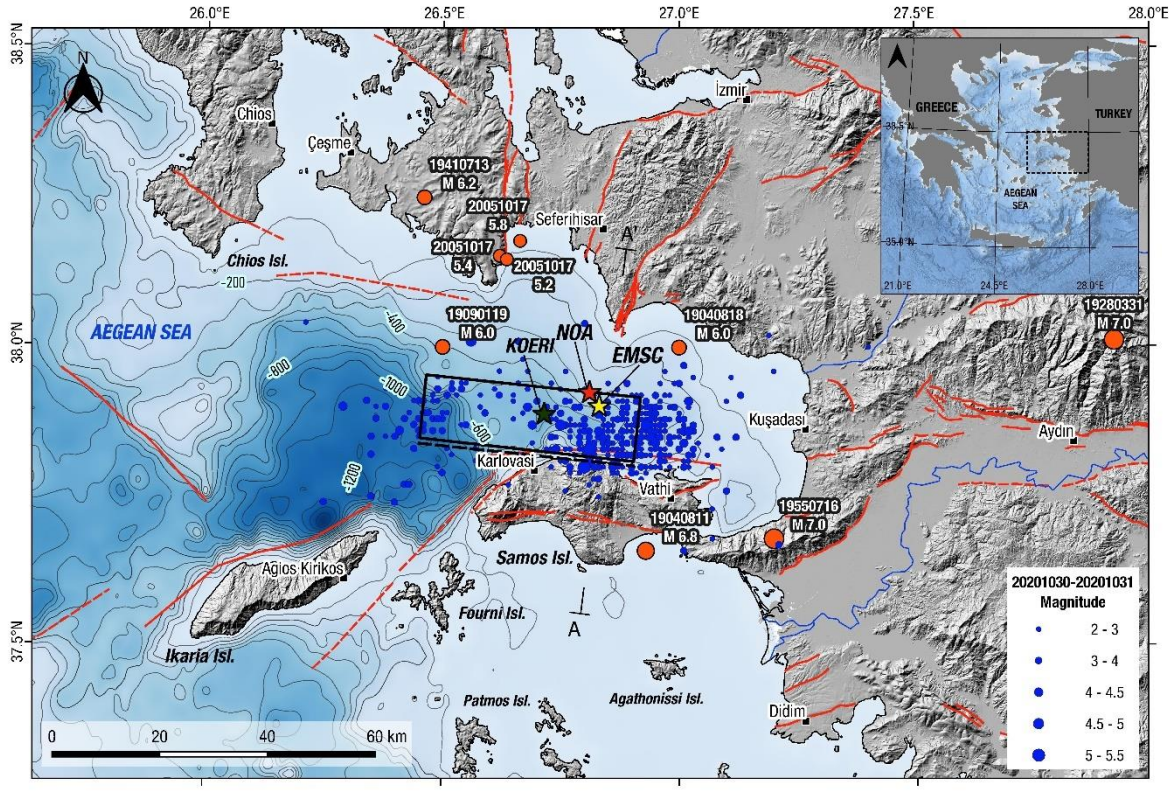

Fig. 1. Shaded relief map of the 30 October 2020 Samos M_w=7.0 earthquake area showing location of the seismic fault determined in this study (black rectangle). Solid stars indicate mainshock epicentres from the National Observatory of Athens (NOA), Kandilli Observatory and Earthquake Institute (KOERI) and the European-Mediterranean Seismological Center (EMSC). Blue dots indicate the first 24-hrs aftershocks from the EMSC catalogue (N=484). Initials A-A' denote the end points of the cross section in Fig. 17. Inset box at upper right shows study area within Greece. Red lines are active faults from the NOAFAULTs database http://doi.org/10.5281/zenodo.3483136

2. The Samos 30 October 2020 earthquake

On 30 October 2020 11:51 UTC a strong and shallow earthquake rocked the eastern Aegean Sea (ITSAK, 2020; Kalogeras et al. 2020; Ganas et al. 2020a; Lekkas et al. 2020; Foumelis et al. 2021; Mavroulis et al. 2021). The epicentre was determined offshore the Greek island of Samos, about 260 km to the East of Athens (Fig. 1). The local magnitude (Richter scale) was measured by NOA as M_L=6.7, while the moment magnitude was calculated by various agencies in the range 6.9 ≤ Mw ≤ 7.0 (see Table 1; Papadimitriou et al. 2020; Kalogeras et al. 2020; Ganas et al. 2020a). The Peak ground acceleration at Vathy, Samos (Fig. 1) reached 0.17 g (Kalogeras et al. 2020). The earthquake triggered a tsunami that caused minor damage at the surrounding islands (Samos, Chios, Ikaria; Fig. 1) and especially in the coastal towns of Vathy (Samos) and Sigacik (Turkey; Kalogeras et al. 2020; Triantafyllou et al. 2021). Immediately after the earthquake field surveys showed coastal uplift at several locations of Samos (Lekkas et al. 2020; Evelpidou et al. 2021; Mavroulis et al. 2021), however, in this study we provide GNSS and InSAR evidence that there was no uplift along the south coast. The focal mechanisms reported by various agencies for the mainshock are listed in Table 1.

Table 1. Focal mechanism solutions reported by various agencies (source: agency websites; see supplementary Text S1 for web sources).

Agency	Time	Lat. (°)	Long. (°)	Depth (Km)	Mag Mw	Strike 1	Dip 1	Rake 1	Strike 2	Dip 2	Rake 2	M_O
AFAD-ERD	11:51:23	37.888	26.777	16.54	6.6	270	46	-91	95	43	-87	3.26E+19
GFZ	11:51:27	37.900	26.820	15	7	272	48	-93	97	41	-85	3.50E+19
GCMT	11:51:34	37.760	26.680	12	7	270	37	-95	96	53	-86	4.01E+19
INGV	11:51:36	37.836	26.808	10.6	7	289	40	-69	82	53	-107	3.90E+19
IPGP	11:51:26	37.897	26.795	14	7	260	36	-116	111	58	-72	3.76E+19
KOERI-RETMC	11:51:24	37.902	26.794	13.1	6.9	272	55	-93	97	84	-85	3.00E+19
UOA	11:51:26	37.920	26.803	13	6.9	270	50	-81	76	41	-101	2.81E+19
NOA	11:51:24	37.900	26.817	6	6.9	294	54	-65	76	43	-120	2.65E+19
OCA	11:51:26	37.910	26.840	10	7.2	275	45	-96	103	45	-85	-
USGS	11:51:44	37.918	26.790	11.5	7	276	29	-88	93	61	-91	4.09E+19

The effects of the earthquake were devastating in Greece and Turkey (Vadaloukas et al. 2020; Cetin et al. 2020). In Greece, two young children lost their lives from a wall collapse in the town of Vathy, eastern Samos (https://edition.cnn.com/europe/live-news/aegean-sea-earthquake-dle-intl/h_9d313a45fc3463479a6ff1ec4da29755). In Turkey more than 100 people died from multiple building collapses in the city of Izmir, ~60-km to the north of the epicentre (Fig. 1; https://en.wikipedia.org/wiki/2020_Aegean_Sea_earthquake).

The Samos earthquake ranged in magnitude 6.6≤M_w≤7.2 (see Table 1 for estimates; excluding AFAD-ERD it becomes 6.9≤M_w≤7.2) and it occurred along a normal fault oriented

E-W as indicated by the moment tensor solutions of both regional and teleseismic data. Until 20 November 2020 06:21 UTC more than 1445 aftershocks (with $2.0 \leq M_L \leq 5.2$) were recorded by the European-Mediterranean Seismological Centre (EMSC; Fig. 2). The mainshock was followed by one moderate-size aftershock, on 30 October 2020 15:14 UTC and with magnitude M_w=5.2. The moment tensor solutions of the mainshock indicate E-W to ESE-WNW normal faulting in agreement with the regional, extensional tectonics (Table 1; Ring et al. 1999; Chatzipetros et al. 2013). The aftershock sequence extends over a E-W distance of ~70-km with most of events occurring east of the mainshock and within a depth range 2-15 km (Fig. 2; see Fig. S1 for a map view). The EMSC aftershock data show an incipient decay the day after the mainshock (Fig. 2a) while the longitude location vs time plot (in days from main shock) shows that the sequence is spatially constrained between 26.4°E – 27.2°E (Fig. 2b); this plot also shows that the sequence is unevenly distributed along strike. Indeed, the data show a peak in seismicity between 26.8° and 27.1°E, a secondary peak immediately to the west and centered at 26.7°E, and a third peak centered at 26.45°E with a clear seismic gap ~26.55°E (Fig. 2c). This uneven and segmented distribution of the aftershocks is established immediately at the start of the aftershock sequence (see aftershock distribution in Fig. 1), and persists over time, even during the most recent periods of lower seismic activity (Fig. 2d; a similar feature is reported by Papadimitriou et al. 2020). This seismicity gap may be due to the complete rupture of the main asperity along the fault plane and subsequent aftershock activity triggering around the co-seismic slip patches (e.g., Atzori et al. 2008; Chiaraluce et l. 2011; Ganas et al. 2019; Melgar et al. 2017, 2020). The E-W extent of the early (24-hr) aftershocks (Fig. 1) is about 55 km, or 1.4 times the size of the modelled fault in this paper (40 km), close to the mean value for the aftershock zone ratio in California (Neo et al. 2020).

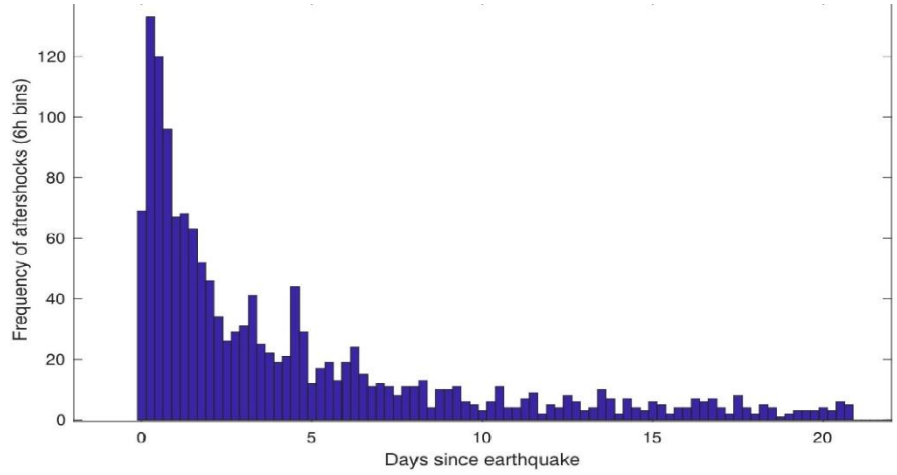
a)
Frequency of aftershocks (6h bins)
Days since earthquake

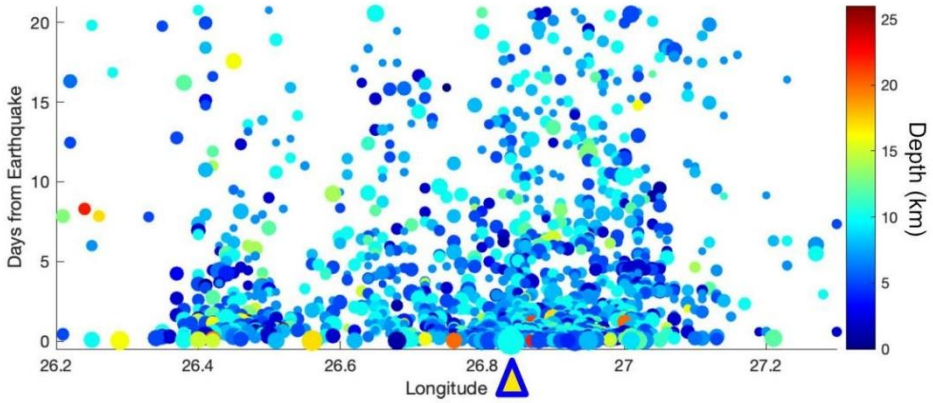
b)
Days from Earthquake
Longitude
Depth (km)

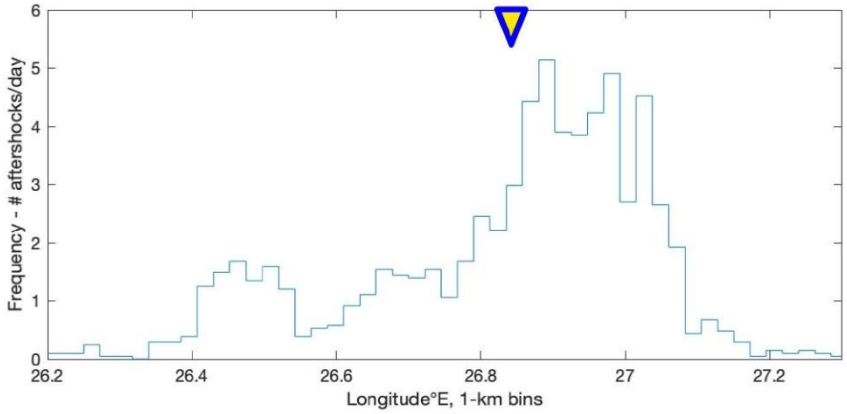
c)
Frequency - # aftershocks/day
Longitude°E, 1-km bins

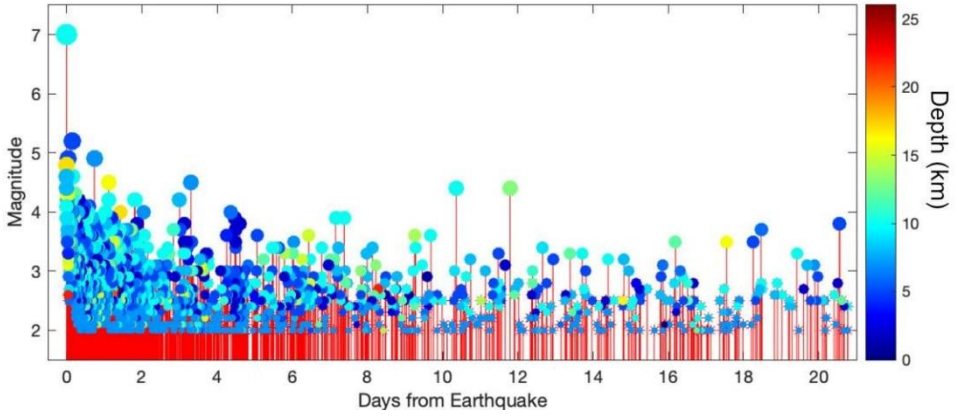
d)
Magnitude
Days from Earthquake
Depth (km)

183

Fig. 2. Spatiotemporal evolution of the Samos aftershock sequence (source of data: EMSC, data until 20 November 2020 N=1445) a) histogram of aftershock frequency of occurrence vs time (6h bins) to show the decay over time b) Daily frequency of occurrence with respect to longitude (east-west) and depth (circle colours correspond to depth, and size to the magnitude) c) histogram of aftershocks in frequency per day along strike (east-west; 1 km bins) d) Magnitude distribution with time and depth. Triangles (yellow with blue outline) in b and c indicate the location of the mainshock for reference.

3. InSAR data processing

We used Synthetic Aperture Radar (SAR) C-band images acquired over the Samos area by the Copernicus European satellites Sentinel-1 from the ascending tracks 29 and 131 and the descending track 36. The first co-seismic, differential interferograms spanning the dates 24-30 October 2020, and 18-30 October, 2020 with images of track 131 (Fig. S2) were calculated on the Geohazards Exploitation Platform (https://geohazards-tep.eu) using the SNAP v5.0 software and were presented in Ganas et al (2020a). The acquisition time of the postseismic image was at 30 October 2020, 16:07 UTC, thus 4 hours & 16 minutes after the mainshock. Then, we produced 17, 15, 17 co-seismic and 10, 6, 6 post-seismic interferograms for each of tracks 131 (ascending), 29 (ascending) and 36 (descending) respectively, using the Automatic Interferometric Processing Station (AIPS; http://aips-p.space.noa.gr/Samos) at NOA. More information on AIPS can be found in text S2. The east, north and up unit vectors, from the ground to the satellites, at the range direction (in the centre or Samos island), are [*-0.680 -0.157 0.716*] for track 29, [*0.629 -0.145 0.764*] for track 36 and *[-0.540 -0.125 0.832*] for track 131. The interferograms captured the ground motion along the line of sight (lLOS; see Look arrows in Fig. S2). These LOS measurements of were used in the inversion model to retrieve the parameters of the seismic fault.

After reviewing all the co-seismic interferograms we decided not to use the track 131 in this paper, because of the better quality of track 29, which is ascending, too. In Fig. 3 we present the best co-seismic interferogram belonging to track 29 and spanning the period 23 October – 10 November 2020. Moreover, we selected the four (4) best interferograms (marked in bold and framed in Table S1) in terms of low tropospheric noise and high coherence of each of the track 29 and 36 (Fig. 4a, 4d). We then unwrapped the interferograms, removing the bias by setting each one of them to a zero mean value. Then, for both the ascending and descending tracks, we averaged the LOS displacement grids these two averaged grids were used for the inversion modelling in section 5. All the following interferograms for which their extent is limited only to the Samos island, are at the notion of post-event minus pre-event, thus phase increasing towards satellite. Fig. S3 demonstrates the increase of signal to noise ratio obtained when using the average interferogram over the best interferogram of track 36 (D), both wrapped and unwrapped.

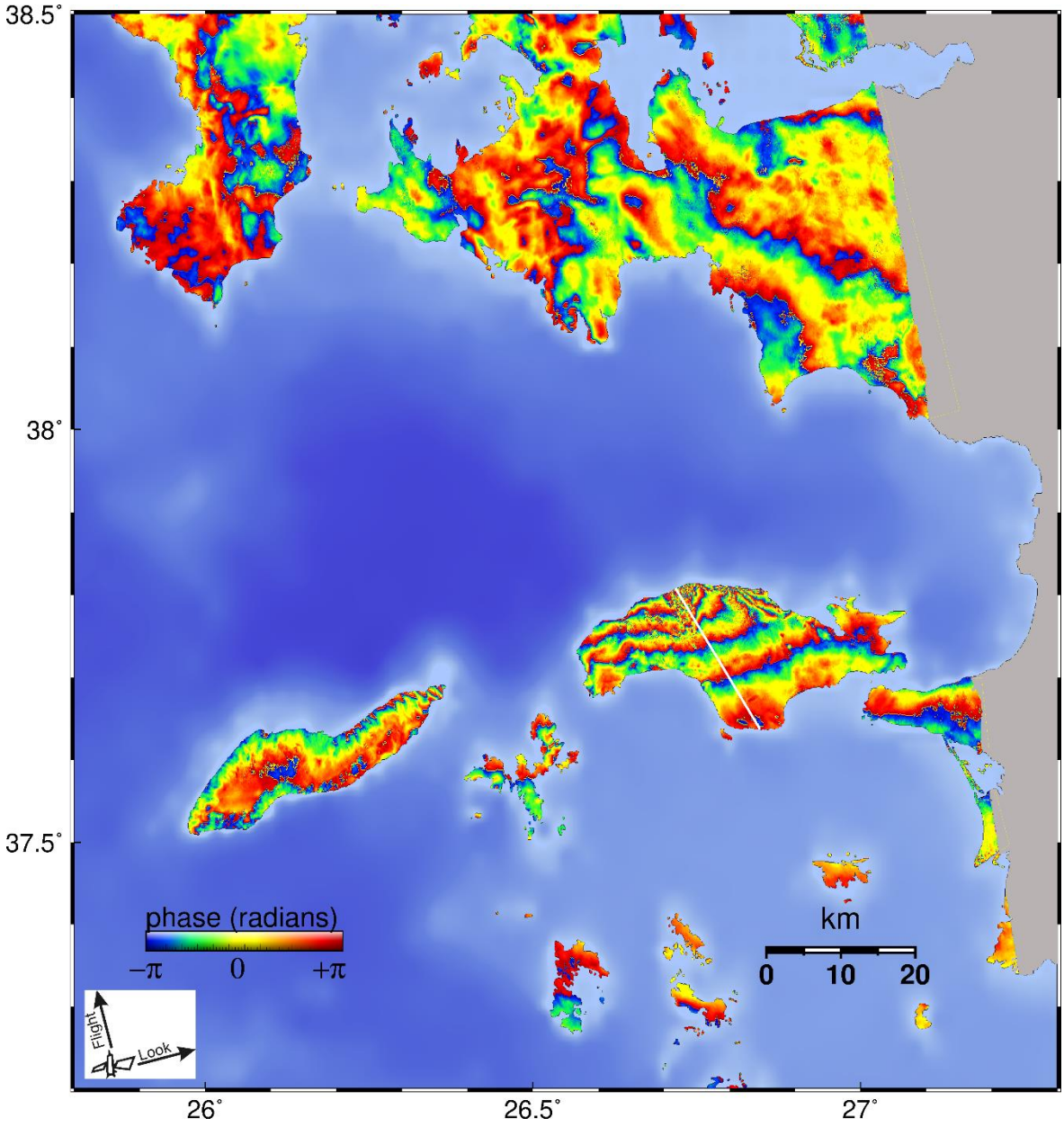

Fig. 3: The best co-seismic differential interferogram calculated with images acquired from ascending track 29 and spanning the period 23 October 2020 – 10 November 2020 (produced by AIPS; grey colour indicates no data). The formation of the interferograms is at the notion of post-event minus pre-event image, thus phase decreasing towards satellite. The fringes in the interferogram onshore Samos show a pattern that supports more the north-dipping fault plane as such concentration requires the vicinity of a fault edge to them. The InSAR data show that most of Samos moved roughly upwards with the exception of a coastal strip (from Agios Konstantinos to Kokkari; see Fig. 9) that moved roughly downwards. Thin white line on Samos indicates location of profile shown in Fig. S9.

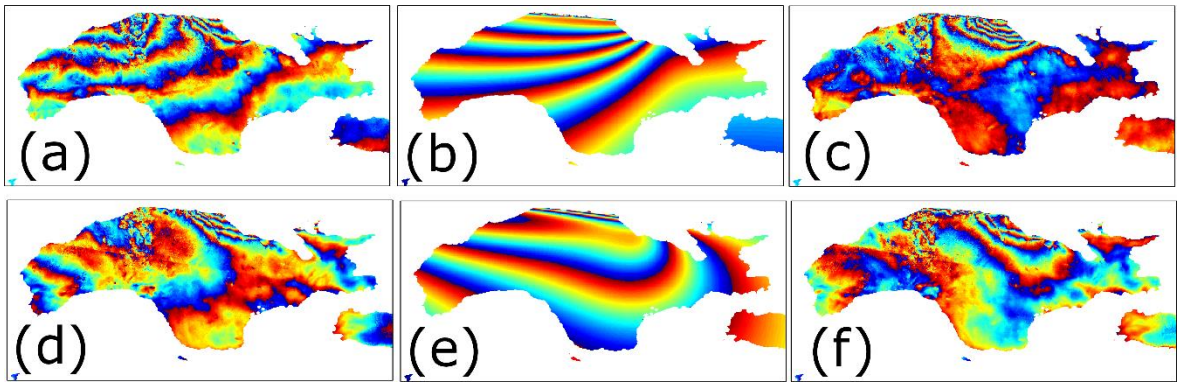

Fig. 4: (a) and (d): Averaged wrapped interferograms for tracks 29 (A) and 36 (D), averaged, (b) and (e) the modelled interferograms of track 29 and 36 and (c) and (f) the residuals.

The interferograms of Fig. 3, Fig. 4, & Fig. S2 show several fringes corresponding to ground deformation onshore Samos. The pattern of deformation shows two main features: an area along the north coast with three fringes oriented ENE-WSW indicating motion away from the satellite (region between Agios Konstantinos and Kokkari; see Fig. 9 for exact locations) and another, larger region mostly in the central and west part of the island with a motion towards the satellite. The absolute value of the interferometric fringes is estimated by anchoring to the LOS the offsets measured at GNSS station SAMU in Vathy (Fig. 1), that is +33 mm for the track 29 and +23 mm for track 36. Considering that the sense of the deformation is the same in both tracks we can infer that the north-northeastern tip of Samos island shows subsidence and the western part of Samos shows an uplift. Accordingly, we proceeded to the extraction of the vertical and east components of the deformation. As InSAR provides only information on two independent LOS measurements (Fig. 4), in order to retrieve the 3-D motion we use as third observation the north component derived from the model that is presented in the next section. The north-south displacements produced by this earthquake are large in the northern Samos, but the weight of the north-south component to the calculation of the LOS displacement is small (between 10-15%). Therefore, our model is sufficient to provide a first order estimate that is accurate enough for constituting the third source of displacement. The vertical and east components of the deformation are shown in Fig. 5 (a and d, respectively). The fact that we can retrieve an accurate measurement of the vertical displacements is particularly important for comparison with the field observations along the shoreline (see section 6) and further geological interpretations.

We interpret the deformation of the central and west part of the island as a result of co-seismic motion along an offshore normal fault, running E-W and dipping to the North. As the rupture is shallow, and the dip angle (from seismology) is significantly different from 45°, the two conjugate planes produce modelled differential interferograms that are not

similar to each other. Therefore, InSAR has the capability to discriminate between the two conjugate planes. Our joint inversion (based on InSAR & GNSS displacement data) approach has resulted in a robust fault model, providing its location, geometry (strike/dip-angle/rake angles and concluding on its dip-direction) and amount of finite slip while assuming a simple and planar fault geometry.

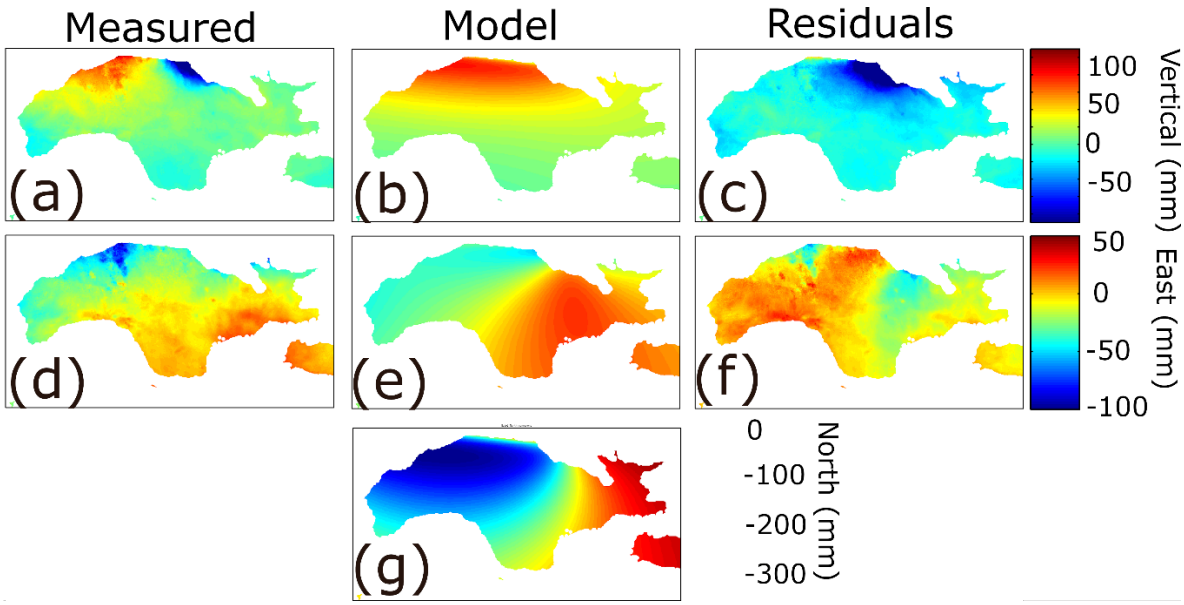

Fig. 5: (a) and (d): The vertical and East components obtained from the averaging of the best interferograms, (b), (e) and (g) the modelled vertical, East and North components and (c) and (f) the residuals. Units in mm.

4. GNSS data processing

Dual-frequency data from fourteen (14) permanent (continuously recording) Global Navigation Satellite System (GNSS) stations were processed. We used GPS observations covering approximately 7-10 days before and after the earthquake (23 October 2020 to 10 November 2020; Table 2 and Fig. 6) in order to obtain position time series and their offsets due to the earthquake. The sampling interval was 30 s, and the data comprise 24-hr daily files. All station records were complete (rejected epochs 0.00%) thus providing substantial observations for mapping the co-seismic displacement field and were included in our processing. The stations belong to the Ktimatologio SA (HEPOS), HxGN SmartNET and Uranus networks of Greece and the Turkish National Permanent GNSS/RTK Network. The azimuthal distribution of the GNSS stations is very good, extending uniformly around the epicentral area (Fig. 6). However, most of the GNSS stations are located more than 50 km away from the epicentre and therefore captured small displacements of the order of a few

cm. The daily coordinates are calculated in ITRF14 (epoch 2020.049) and converted to Universal Transverse Mercator UTM (North) zone 35. Their uncertainties were converted onto the local geodetic frame, based on the given Cartesian (ECEF; earth-centered, earth-fixed) sigma (95%) ones.

The processing was made with the Precise Point Positioning (PPP) strategy by means of the GIPSY/OASIS II software (version 6.4) developed by the Jet Propulsion Laboratory (JPL; http://gipsy-oasis.jpl.nasa.gov). We used the JPL final satellite orbits (flinnR) and clocks, absolute antenna calibration, random walk troposphere estimation, and the FES2004 ocean loading model. We calculated the static offsets (and their uncertainties) for the 30 October 2020 event (Table 2 & Table S2; Fig. 7 and Fig. S4a & S4b). The offsets indicate cm size motion mainly along the N-S direction. Station SAMO (Fig. 6) registered the largest displacements as it moved 35.6 cm towards south and 3 cm towards west. In terms of Up-Down (vertical) displacement we obtained clear trends of co-seismic motion for the three stations located onshore Samos (SAMO, 093A & SAMU) with amplitudes +8.2, +2.3 and +2.1 cm, respectively.. The vertical displacements at the GNSS stations enhance the robustness of the north-dipping fault model as they allow to discriminate between the two conjugate focal planes (see also synthetic models of Okada-type dislocations; Okada, 1985) in Fig. S5. Regarding the large aftershock on 30 Oct. 2020 15:14 UTC (M=5.2; located 9 km to the N of Samos, NOA solution), we could not find any evidence of this aftershock in the GNSS time series. Furthermore, the GNSS time series of SAMU and SAMO stations show the existence of a small post-seismic motion in the days following the mainshock (Fig. 7). This postseismic motion leads to drifts of LOS values in our interferograms that we can estimate. The values of those drifts is low so we can assess that the interferograms presented in Fig. 2, 3 & 4 are not biased by post-seismic motions and represent well the co-seismic signal of the earthquake.

Table 2. List of co-seismic offsets (in mm) determined by PPP processing. Columns dE, dN, dUp show displacements (East, North, Up) and mE, mN, mU the modelled values, respectively. The uncertainties of E, N, Up displacements are reported in Table S2. The GNSS stations are shown in Fig. 6.

Station	Lat. (°)	Long. (°)	dE	dN	dU	mE	mN	mU
SAMO	37.7927	26.7053	-30	-356	82	-38	-348	75
SAMU	37.7575	26.9734	-5	-64	21	4	-57	30
093A	37.6716	26.8334	22	-152	23	11	-167	8
CHIO	38.3679	26.1272	-8	17	2	-7	19	2
CHIU	38.3665	26.1359	-8	18	5	-7	19	2
IKAR	37.6282	26.2243	-7	-31	7	-18	-34	4
IKAU	37.6055	26.2733	-4	-48	4	-21	-43	3

KALU	36.9624	26.9617	3	-14	-3	1	-15	-2
LERO	37.1364	26.8545	3	-20	-	1	-24	-
KALY	36.9558	26.9762	3	-11	-1	1	-15	-2
AYD1	37.8407	27.8378	0	7	-	0	1	-
CESM	38.3038	26.3726	-12	54	-	-12	48	-
IZMI	38.3948	27.0819	10	30	2	13	36	-2
DIDI	37.3721	27.2687	2	-5	-	5	-15	-

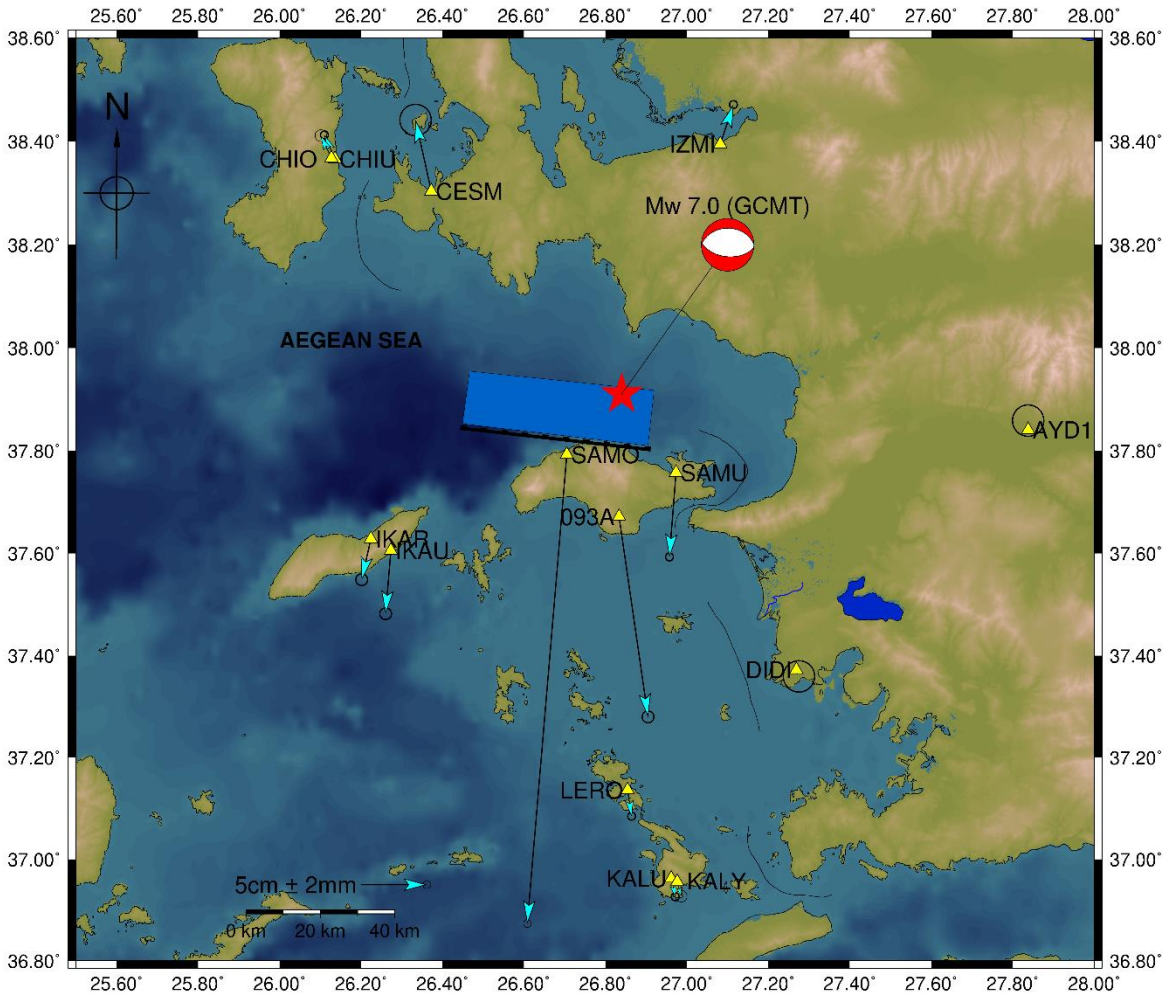

Fig. 6: GNSS co-seismic displacement map showing also topography/bathymetry, the focal mechanism (beachball; compressional quadrants in red) and the epicentre of the Samos October 30, 2019 earthquake. Blue rectangle indicates the surface projection of the seismic fault (thick black line is the upper edge with boxes on the downthrown side). Triangles indicate permanent GNSS station locations. Vectors indicate horizontal displacement of GNSS stations with 67% confidence scaling.

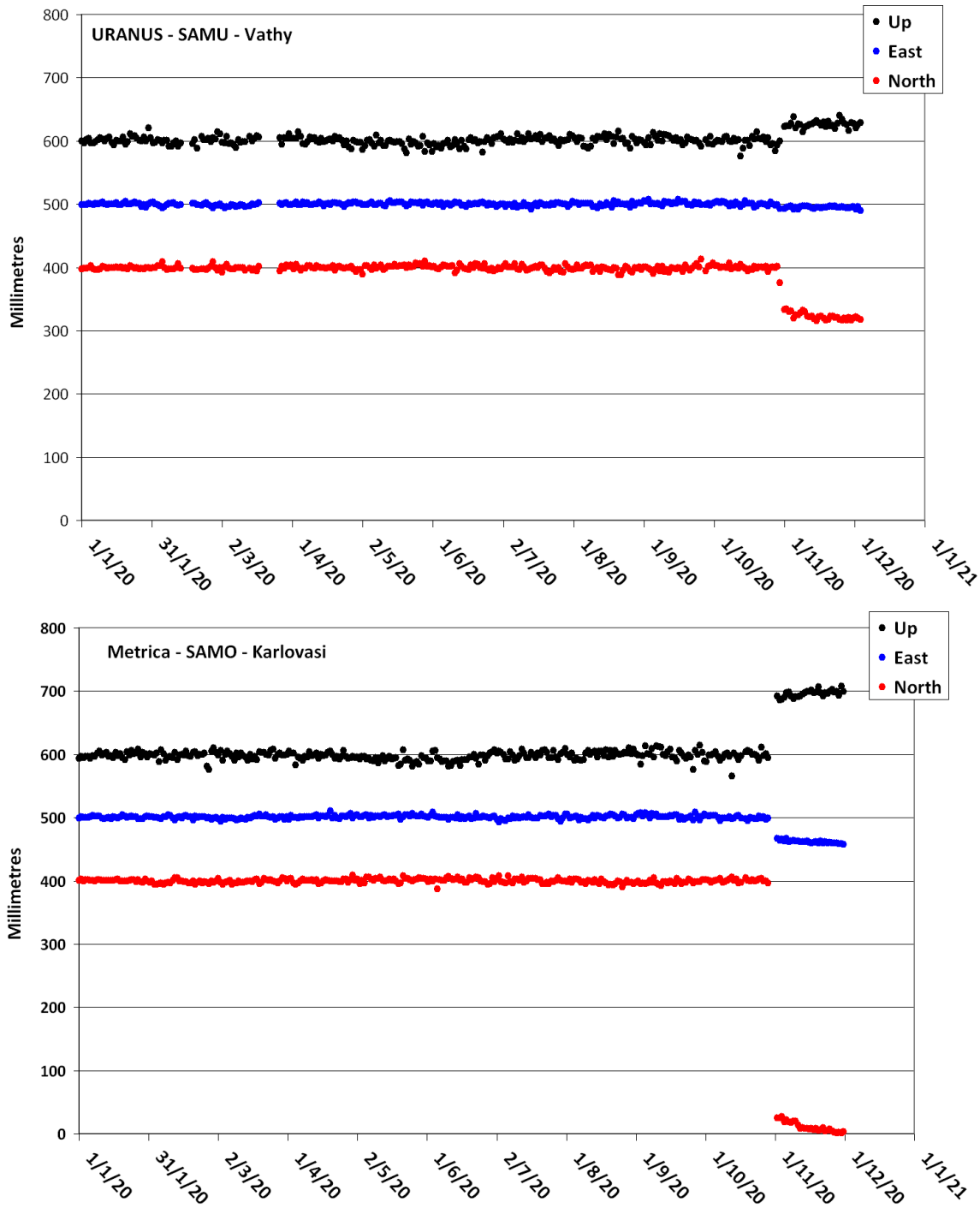

329

330 **Fig. 7**. Position time-series of stations SAMU (Vathy) and SAMO (Karlovasi) (E, N, Up in blue,
331 red, black dots, respectively). The time-series have been offset for clarity on the Y-axis. The
332 small post-seismic signal is visible mainly in the North-South component. Station locations
333 are shown in Fig. 6.

334

5. Joint inversion of geodetic data – fault model

We inverted the geodetic data (InSAR and GNSS) assuming a half-space elastic model with uniform slip along a rectangular fault surface, using the code *inverse6* (Briole, 2017). For the modelling of the InSAR data, the same weight was given to the ascending and descending picks. The ascending and descending observations (fringe pickings), here 64 for the ascending track 29 and 33 for the descending track 36, thus the weight ratio descending over ascending is 5/10. The 99 data points are compared against the model in Table S3 (see Fig. S6 for location of picked fringes). We then used the 14 sets of GNSS offsets (horizontal and vertical; Table 2) weighting 10 times more the horizontal offsets than the vertical ones and the InSAR data. The root mean square (r.m.s) scatter between data and model is 6.4 mm for the GPS horizontal data, 9.8 mm for the GPS vertical data and between 23 - 59 mm for the InSAR data (see Table 4 for model performance), respectively. We tuned the model in favor of GNSS horizontal with the ratio 6:1 because of the higher reliability of the horizontal GNSS displacements and their broad coverage, while InSAR is confined inland Samos, which is, in particular, the reason for the weak constraint on the fault length from InSAR only.

The geodetic observations presented above imply clearly and unambiguously that the seismic fault plane is the one dipping towards north (Fig. 8). Indeed, there is no solution with the antithetic plane that can fit correctly both GNSS and InSAR at the same time. Moreover, the north-dipping plane is consistent with the submarine geomorphology (e.g. Mascle and Martin, 1990; Nomikou et al. 2021) and the tectonic context of the area.. At a local scale there are two to three fringes showing motion away from the satellite in the coastal area between Agios Konstantinos and Kokkari; (Fig. 4; see Fig. 9 for locations) that cannot be modelled with our simple model of uniform slip on a single fault plane. We suggest that they were formed because of a “local effect” due to the complexity and possibly the non-planarity of the mainshock rupture near its eastern termination. We also considered the case of a “deep-seated” gravitational instability that was induced due to strong ground shaking but the size of the feature (nearly 6-km E-W) and the shape of the fringes seem to rule it out. Moreover, there are no clearly defined boundaries of the local deformation visible in the interferograms, and the coastal area covered by this pattern changes in different orbit interferograms, thus hinting at a tectonic source.

We started the inversion for the East, North, Up coordinates of the fault-top centre and for the fault length. We did not invert for the dip, and rake angles, assuming 37°, and -90° respectively, i.e., using the GCMT solution which is consistent (±2°) to our geodetic solutions for previous events in the Aegean Sea (i.e. Kos, 2017; Zakynthos, 2018; Durres, 2019; Ganas et al. 2019, 2020b, 2020c). The 37° dip-angle is close to the average (39°) of the teleseismic determinations of the focal mechanism parameters (see Table 1; also, the 37° angle fits the hypocentre determinations from regional networks, see Fig. 17 below).

The InSAR data alone do not allow to invert for the fault azimuth because of their insufficient spatial coverage but thanks to the existence of the GNSS data we inverted for the azimuth, too. We have not tried to constrain the rake of the slip vector, as we know that in the modelling of InSAR (and also GNSS), there is a strong trade-off between rake and azimuth angles. Therefore, we considered that it was more rigorous to rely on the angles provided by seismology through the focal mechanisms; rake angle between [-116° / -65°], median -92°, and azimuth [260°/ 294°], median 272°. Considering the fault as pure normal (rake -90°) we inverted only for the azimuth (strike) with small relaxation. In Fig. S7 we see that it is inverted to 276°±1°. Indeed, there is a strong agreement between the azimuth of the modelled fault and orientation of the known active structures (see active faults in Fig. 1).

Concerning the location of the fault, we obtained robust estimates on the 3D position of the top-fault centre (uncertainty of 0.7 km, 0.5 km and 0.3 km in east, north, vertical, respectively), i.e., the horizontal coordinates are well constrained by InSAR displacement data and the vertical coordinates are also well constrained by the gradient of the InSAR fringes. The best-fitting length was 40±3 km (Fig. S7). Like for azimuth and rake, there is also a trade-off between the amount of slip and the fault width. The best-fitting depth to top-fault was 0.6±0.3 km and the fault width 15±3 km. Non-planar fault solutions were not tested as the GNSS and InSAR data do not have sufficient coverage in the near field of this offshore fault..

The fault parameters were used to construct a synthetic interferogram which is shown in Fig. 8 (ascending orbit) and Fig. S8 (descending orbit), respectively (also shown are the fault projection to the surface and the measured and modelled horizontal co-seismic GPS vectors). The modelled GNSS displacements agree well with the observed GPS data (Table 2, Fig 6, Fig. 8, Fig. S8). We also present the residuals of the InSAR vertical and east components and the north component model In Fig. 5c and Fig. 5e, respectively. As mentioned earlier the negative residuals in Fig. 5e are due to the unmodelled ”rupture complexity” effect along part of the northern coastline (Agios Konstandinos to Vourliotes; Fig. 9). We also drew a 21-km long NNW-SSE displacement profile (Fig. S9; the profile location is shown in Fig. 3) over central Samos in order to compare LOS InSAR vs modelled values and we obtained an average difference of 5.5 mm between the two sets (the standard deviation is 8 mm). In terms of earthquake size, the geodetic moment (Mo) is calculated to 3.06 10^{19} N m assuming a rigidity of the medium of 3.0 10^{10} Pa. This value is close to the median of the seismological one which is 3.5 10^{19} N m. The fault parameters are presented in Table 3 in comparison to the parameters obtained using only ascending orbit data (Ganas et al. 2020a).

The geodetic data does not allow to constrain multiple patches on the fault plane. This is due to the fact that the fault is offshore, thus without geodetic constraints in the near field (on its hangingwall). However, the aftershock distribution along the fault (in an E-W

direction, Figs. 2b and c), shows a clear differentiation that may be related to either a) a fault geometry that is more complex than the simple planar fault that we have adopted here, and/or b) that the finite displacement is unevenly distributed along strike. Seismicity data alone, however, do not have the required precision in location to clearly delineate the geometry of the seismogenic fault (see also seismicity cross-sections in Papadimitriou et al. 2020 and Foumelis et al. 2021).

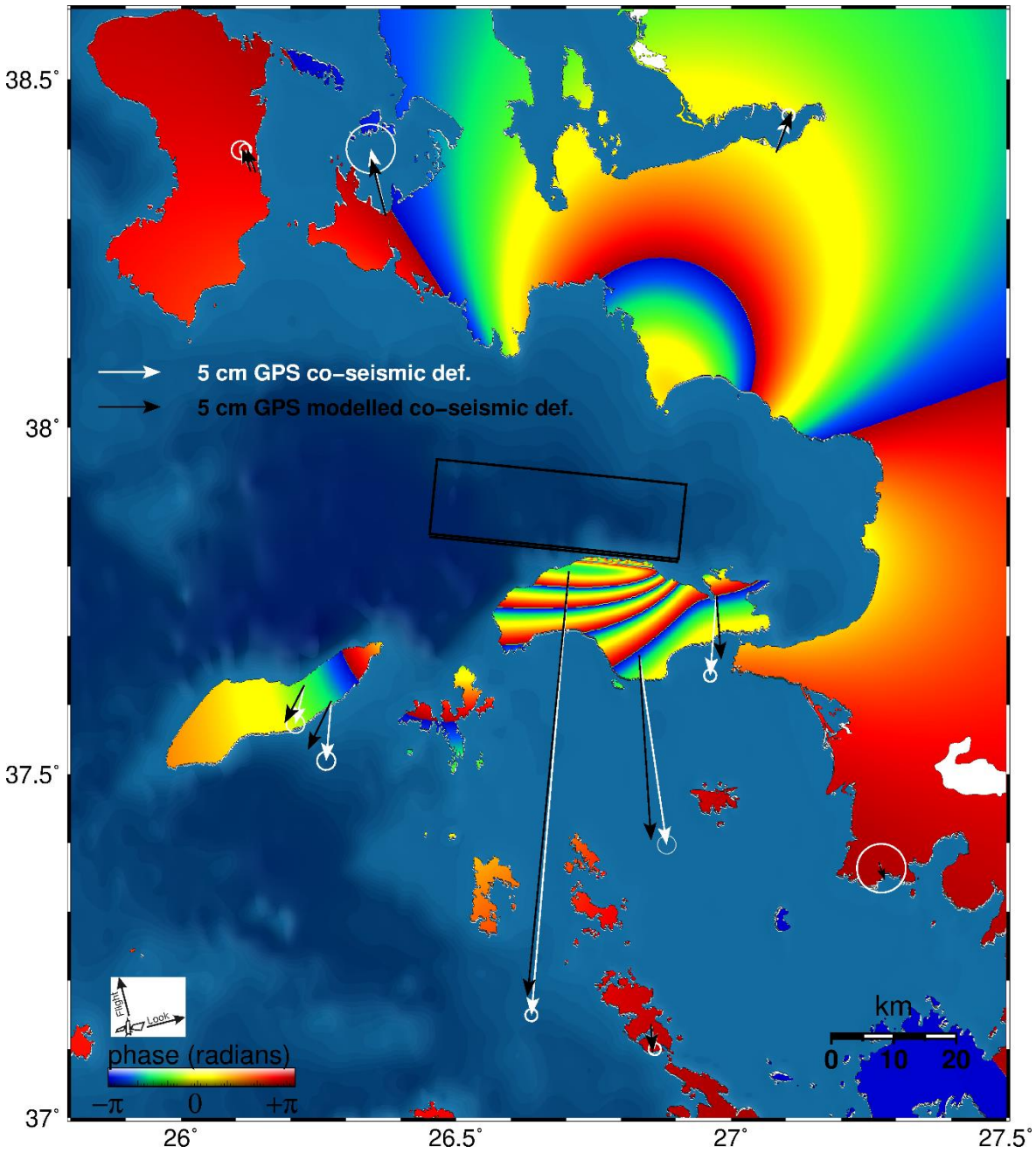

Fig. 8: Map showing a synthetic interferogram (ascending orbit). The black rectangle indicates the surface projection of the modelled fault (dip-direction is towards north). Arrows indicate GPS offset vectors (observed vs. predicted; see Table 2). The formation of

424 the synthetic interferogram is at the convention of post-event minus pre-event, thus phase
425 decreasing towards satellite.

426

427 **Table 3.** List of fault parameters after inversion of geodetic data.

	Ganas et al. 2020a	**This study**
Number of inversions	2267	5610
M_o (N-m) – geodetic	3.5e+19	3.06e+19
Mw	7.0	7.0
R.m.s (total, weighted)	16.3	13.0
Centre of Top-fault LON (°)	26.707	26.6784
Centre of Top-fault LAT (°)	37.827	37.8290
Azimuth – strike (°)	N276E	N276E ± 1
Centre of Top-Fault Depth – km	0.9	0.6 ± 0.3
Length – km	36	40 ± 3
Width – km	18	15 ± 3
Dip (°)	37	37 (not inverted)
Normal slip (m)	1.8	1.7 ± 0.4
Strike slip (mm)	0	0 (not inverted)
rms InSAR ascending (mm) on pickings		50.2
rms InSAR descending (mm) on pickings		30.5
rms InSAR east component		23
Rms InSAR vertical component		23
Rms InSAR LOS ascending (mm) on whole Samos		50
Rms InSAR LOS descending (mm) on whole Samos		59
rms GPS vertical (mm)		9.8
rms GPS horizontal (mm)		6.4

428

429 With a fault dip-angle assumed to be 37°, the top-edge of the fault at 0.6 ± 0.3 km, and a
430 width of 15 ± 3 km, the root of the fault is located at a depth of 9.6 ± 2 km, and the geodetic

centroid depth is at 5.1 ± 2 km. This depth of the fault root is consistent with the 10-13 km range of hypocentre depths determined by USGS, OCA, KOERI, INGV (see Table 1) and Papadimitriou et al. (2020). For the Kos 2017 M6.6 event with a similar north-dipping geometry we estimated the fault root at 10 km (Ganas et al. 2019).

6. Earthquake Environmental Effects

The environmental effects of the 30 October 2020 include rock falls, rock slides, landslides, road-fill failures, coastal uplift and small-size liquefaction features (see also Lekkas et al. 2020; Foumelis et al. 2021; Mavroulis et al. 2021). The data were collected during a field survey that took place on 6-8 November 2020, one week after the occurrence of the earthquake. We were able to timely record the triggered geo-environmental effects (mainly slope failures and liquefaction). The areas affected by these phenomena are mainly found on the northern coastline of the island (Fig. 9) such as a) the villages of Avlakia, Kokkari and the town of Vathy on the east and b) by the coastal zone from Agios Konstantinos to Karlovasi to the west (Fig. 9). Regarding the other parts of the island, the earthquake triggered only sparse and small size rock falls and rock slides on sites very prone to slope failures. In particular, liquefaction phenomena such as sand craters and ejection of fine-grained sand through ground cracks were documented at the coastal site of Malagari beach, on the NW edge of the Vathy bay (Fig. 10a). Additional environmental effects were mapped over Samos island using Copernicus Sentinel-2 & Maxar WorldView optical satellite imagery. A map showing the spatial distribution of earthquake-induced failures is shown in Fig. 9, while the coordinates of the field-documented failures are listed at Table S4.

We observed that the dominant geological effects triggered by the earthquake are related to slope failures. In particular, rock falls and slides, and shallow and deep-seated landslides were mapped on the northern and western part of the island and at the Karlovassi hinterland area, on both natural and cut slopes. In several cases we observed that the failures are associated with pre-existing tectonic discontinuities (faults, joints) and steep slopes within heavily fractured sedimentary rocks e.g., limestones (as is the case in Avlakia where sliding occurred along a steep, northeast-facing slope with northeast-dipping limestone strata; the dip angle was measured by AG between 51 and 53°). Moreover, no primary fault surface ruptures were observed in the field which is consistent with the off-shore fault location determined by geodesy (Fig. 8).

The liquefaction site at Malagari beach (Fig. 10a) is a few metres away to a coastal site which subsided as it is evidenced by the partial submergence of a coastal tree line, that was located along the beach (approximately oriented N-S). Part of the beach is now under water with preliminary measurements indicating a maximum subsidence of 53 cm (Fig. 10b, c, d).

We suggest that this is due to strong ground shaking that induced lateral spreading of the surface soil horizons.

Additional data were provided by the InSAR images that showed extensive decorrelation in the hilly area both east and south of Karlovasi (Fig. 11). The InSAR images indicate chaotic structures that formed inside valleys (Fig. 12). As the structure is clear on all co-seismic pair combinations (including the 30 October 2020 scene) it is evident that it does not represent a tropospheric effect between the SAR acquisitions or an artefact of the DEM used to make the interferograms. We mapped a convergent pattern of motion (Fig. 11a) inside the main valley to the east of Neo Karlovassi (Fig. 12) that we interpret as a gravitational feature than a primary (seismic) one.

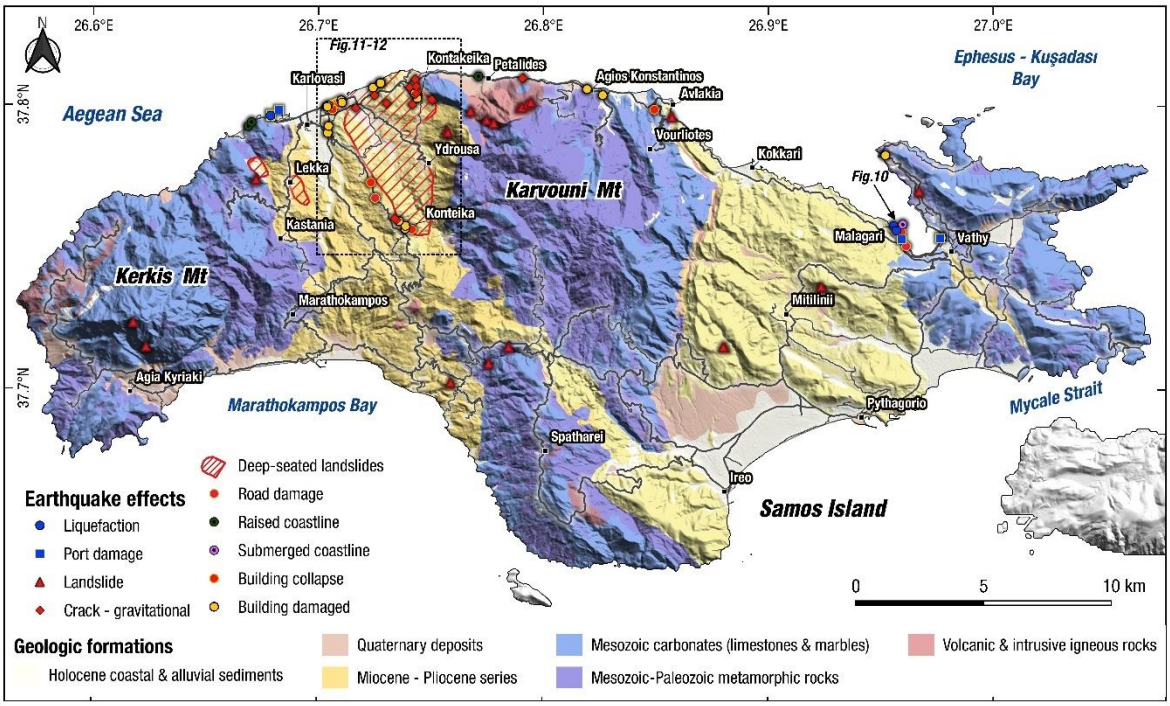

Fig. 9. Locations of mapped earthquake environmental effects of the October 30 earthquake over Samos island (6-8 November 2020 field survey). Arrow shows location of Fig. 10. Box shows extent of Fig. 11 & 12. Background geology is a simplified version of the geological map of Theodoropoulos (1979).

Fig. 10. Field photographs showing earthquake-induced failures at Malagari, Samos (see Fig. 9 for its location, opposite to the town of Vathy) a) liquefaction b) coastal subsidence of 53 cm c) submergence of former beach d) submerged tree line.

Both InSAR and optical satellite data support this interpretation as a set of massive, deep-seated gravitational displacements (DSGD; e.g. Moro et al. 2011), distributed along the western and eastern slopes of the Neo Karlovassi valley, that were triggered during the 30 October 2020 earthquake. The decomposed unwrapped interferograms (East – West component; Fig. 11b) document the converging motion of the ground surface and show the extent of triggered landslides. The valley also contains huge (1-4 km) paleo-landslide complexes visible in optical satellite images and the digital elevation model, parts of which were activated (Fig. 12). Most clear earthquake-induced landslide cases are the one up-stream from Neo Karlovasi (interpreted as a Pliocene limestone cap that slided along ENE-dipping beds; Fig. 13), and the area north of village Kontakeika towards the coast, on the other side of the valley (Fig. 12). The deformation and offsets from the main activated landslide complex near Kontakeika are also visible along the coastal road network and they were confirmed by field inspection on November 6, 2020 (Fig. 11 c,d). Due to the small amount of displacement of the triggered DSGDs, field evidence is limited to local tensional fractures perpendicular to the slide movement axis, and ground cracks along its boundaries (Fig. 11d). Co-seismic triggering of large deep-seated landslides is a common occurrence

during shallow earthquakes, and are frequently observed through mainly geodesic imaging due to the small amount of displacement involved (Moro et al. 2011; Lacroix et al. 2014; Lacroix et al. 2020).

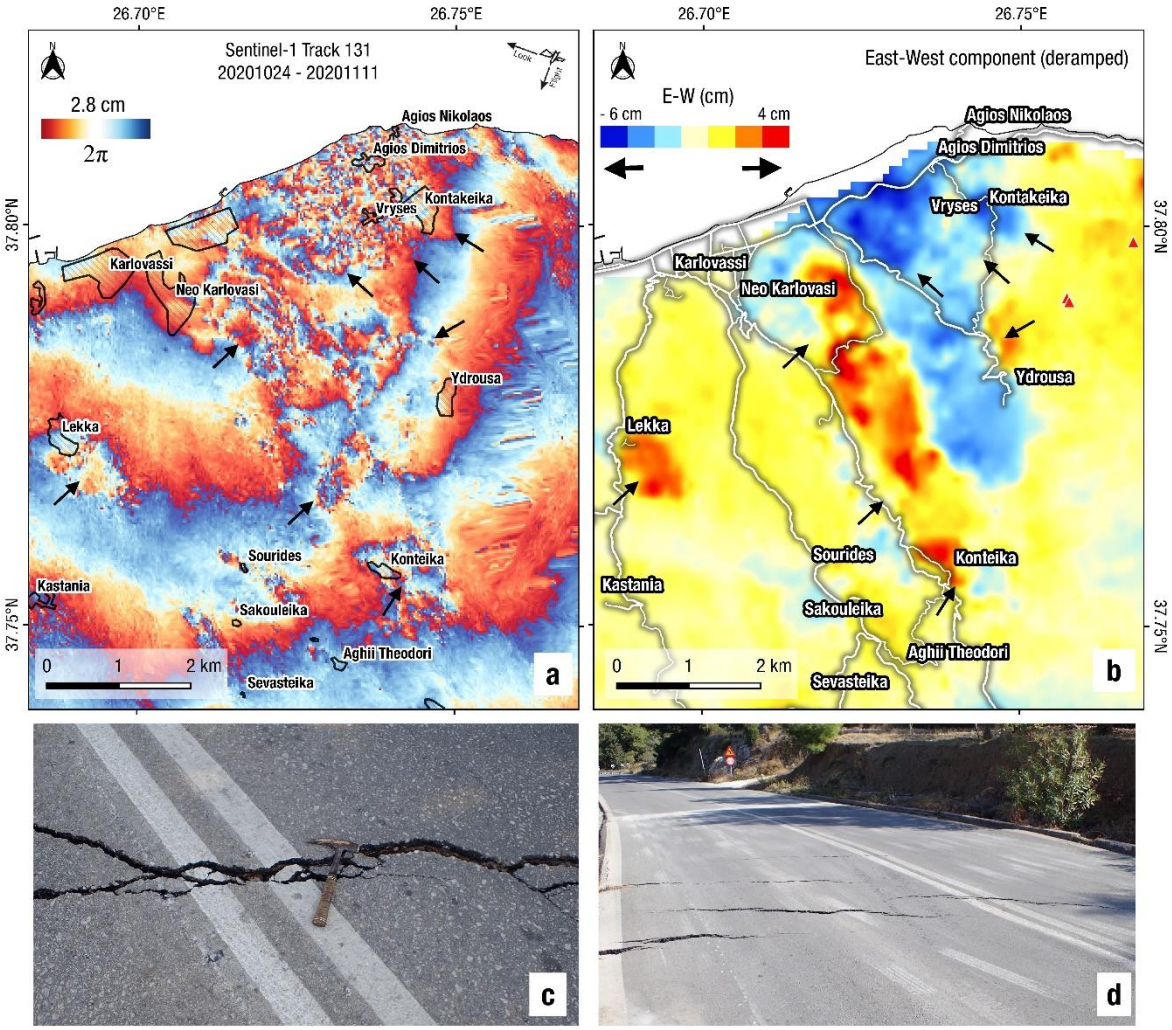

Fig. 11. Maps showing co-seismic landslide activity around Karlovasi, evident in Sentinel-1 differential interferograms. De-correlated areas and fringe patterns mark the location of DSGDs (black arrows) in descending (a) interferogram. Decomposed unwrapped interferograms (East – West component) show the extent of triggered landslides (b). The E-W displacement raster image was deramped around the landslide area in order to diminish the co-seismic displacement effect and to enhance movement along the eastern and western slopes. c & d) Field photos of ground cracks along the boundaries of activated landslides (see Table S4 for coordinates).

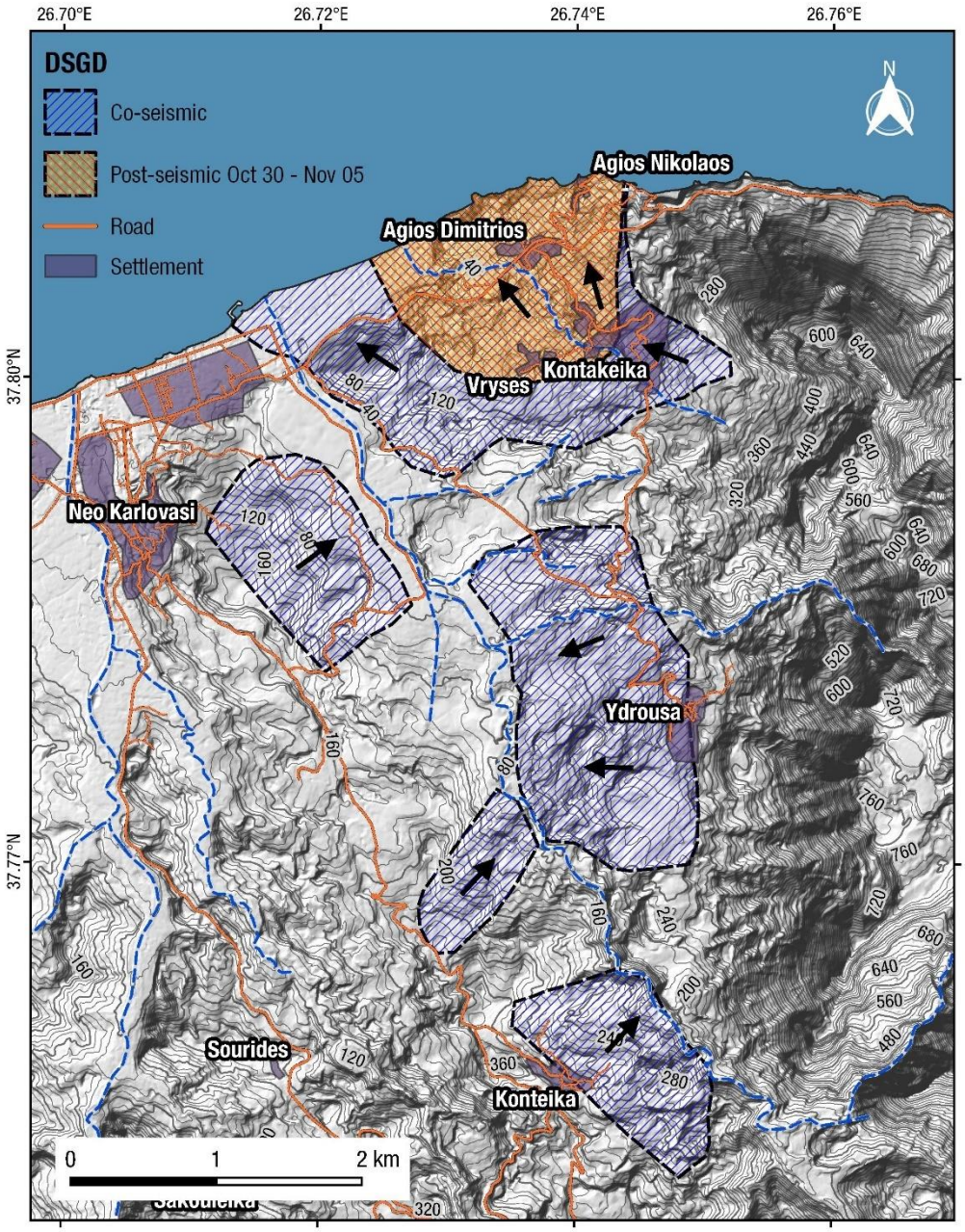

520

521 **Fig. 12**. Shaded relief map of the valley to the east of Karlovasi where deep-seated
522 gravitational displacements (DSGD) were observed both in InSAR images (Fig. 11) and in
523 the field. The activated slides are delineated by polygons, along both sides of the valley.
524 Northernmost structure (orange) showed displacement during the early post-seismic
525 period (30 October – 5 November 2020). Contour interval is 10 m.

526

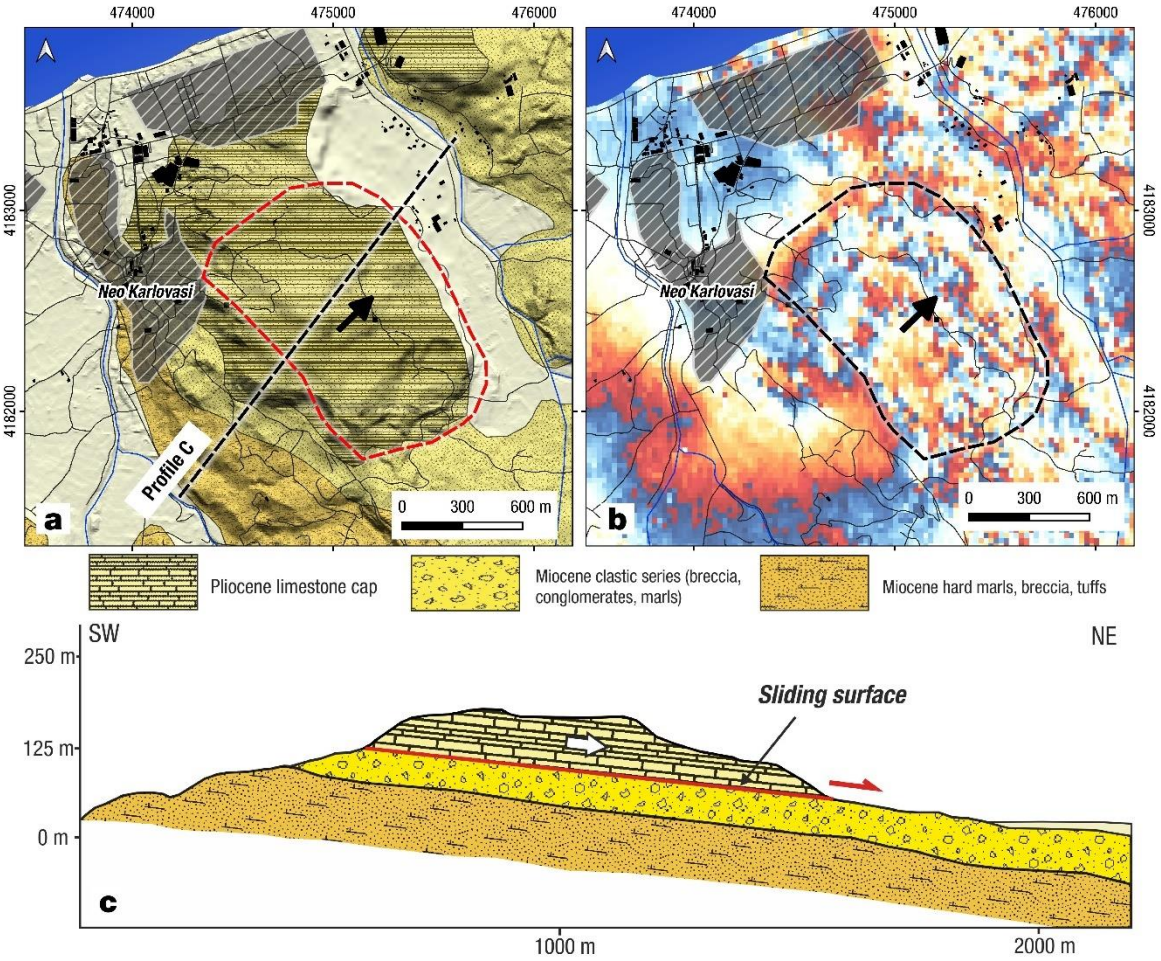

527

528 **Fig. 13**. Geological map (a; Theodoropoulos, 1979), InSAR interferogram of the image pair
529 23 October – 4 November 2020 (b) and cross-section (c) of earthquake-induced slide to
530 the SE of Neo Karlovassi, Samos. The sliding surface is located at the base of the Pliocene
531 limestone beds that overlie the Miocene clastic series of western Samos.

532

533 **7. Discussion-Conclusions**

534 **7.1 Postseismic deformation of the footwall and relation of co-seismic to post-seismic**
535 **slip**

536

537 One of the important aspects of the Samos earthquake is that it is one of a few cases of
538 normal-slip earthquakes where we can accurately measure postseismic deformation of the
539 footwall block. This is possible because of the magnitude of the mainshock (M_w=7.0) and
540 of the existence of sufficient geodetic data. The two GNSS stations (SAMU & SAMO) that
541 were situated on the footwall close to the fault (Fig. 6) have provided accurate information
542 on ground deformation during both the co-seismic and the post-seismic phases (during the
543 first 10-days; Fig. 14 and Table 4). The earthquake produced a significant amount of post-

seismic displacement in the near field (a few km from the top-fault edge; Fig. 14), detected by the two stations; larger in SAMO with a few cm amplitude, a horizontal motion of -4.4 cm (North-South component) and 1.8 cm of uplift; Table 4). In SAMU, located 24 km towards East, the postseismic motion was 1.6 cm and 0.7 cm, respectively. The ratio of the postseismic to co-seismic motion per station is 12-25% (north-south component) and 22-33% (on the vertical component). Interestingly we observe that the co-seismic and post-seismic vectors are not aligned; the SAMO station shows a motion towards N202°E during the postseismic period as opposed to N185°E during the co-seismic one. The fastest part of the postseismic motion lasted until 10 November 2020, that is 11 days (Fig. 14 inset). Then, the decay was slower until the 1st of December 2020 where we cannot see it anymore because of data being comparable to noise (Fig. 14 inset). Thus, the duration of the detectable post-seismic signal is 30 days which is measured on the horizontal component of station SAMO. This value is close to the 21 days we found in the case of the M_w=6.7 Zakynthos earthquake (Ganas et al. 2020b). It is reasonable to suggest that the cause of the deformation is shallow afterslip along the rupture plane of the mainshock as it has been documented in other similar ruptures (e.g., Cheloni et al. 2014; Pousse-Beltran et al. 2020; Briole et al. 2021). Shallow afterslip near the top-edge of the rupture plane may be responsible for the early aftershocks (24-hr) that are aligned along Samos's north coast (Fig. 1). For capturing the full pattern of the fast post-seismic motion that lasts just a few weeks it would have been necessary to deploy in the field additional GNSS stations which were not available. This would be also necessary to fully capture the flexure of the footwall away from the rupture (e.g., Fernandez-Blanco et al. 2020), as our data (Fig. 15) plot on the flat part of the vertical displacement profile.

Table 4. Estimation of seismic displacements at stations SAMU and SAMO and their InSAR equivalents. Ratio is the post-seismic displacement divided by the cos-seismic one. The post-seismic data refer to the first 10-day period following the mainshock.

Station	**dE (mm)**	**dN (mm)**	**dU (mm)**	**l.o.s (mm) track 29**	**l.o.s (mm) track 36**
SAMU co-seismic	-5	-64	21	33	23
SAMU post-seismic	0	-16	7	8	8
SAMO co-seismic	-30	-356	82	155	82
SAMO post-seismic	-11	-44	18	27	13
SAMU ratio	0	0.25	0.33	0.24	0.35
SAMO ratio	0.36	0.12	0.22	0.17	0.16

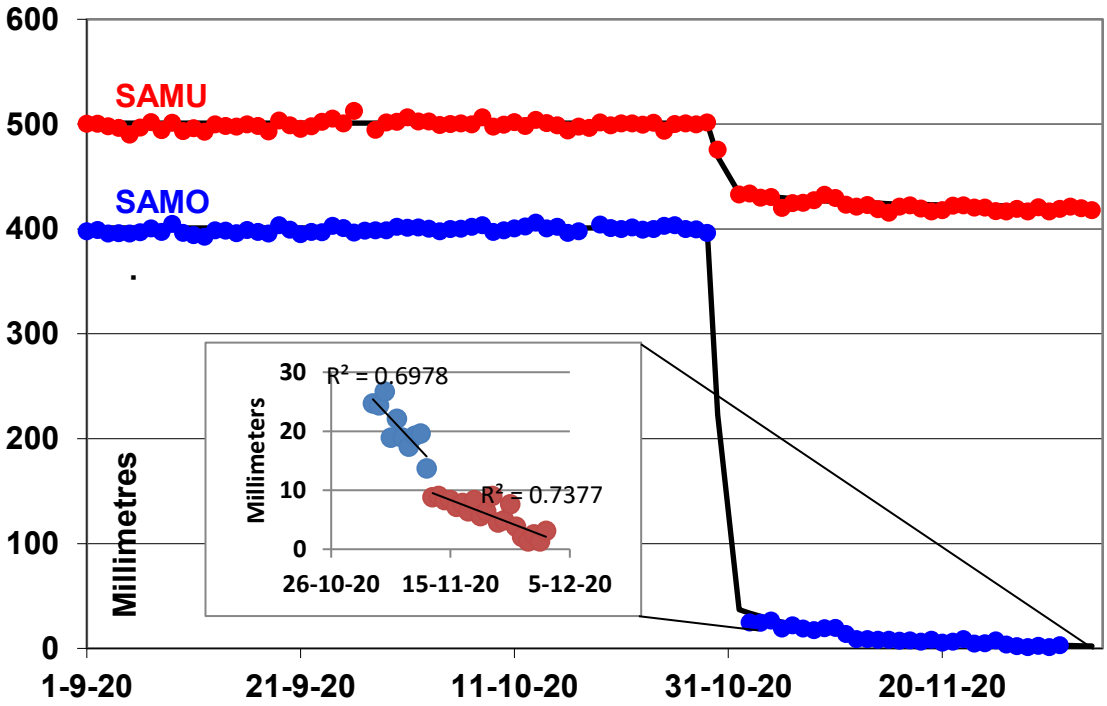

574

575 **Fig. 14**. Time series of North coordinates of station SAMO (Karlovasi; blue dots) and SAMU
576 (Vathy; red dots). The inset box shows the post-seismic period of SAMO with a break in
577 slope around 11 November 2020, thus signifying the end of the fast term of the post-
578 seismic motion.

579

580 We also detected postseismic motions in the InSAR data (as did Foumelis et al. 2021), in
581 particular a post-seismic signal is visible on track 131, that was acquired on the same day,
582 ~4h15' after the mainshock. In three out of five postseismic interferograms having as
583 primary image (master) this particular acquisition, one fringe is visible, spread out in the
584 north of the island, with the same direction of motion (LOS) with that of the co-seismic
585 ones. To compare with the GPS data (Table 4), the postseismic difference in the LOS of
586 pixels enclosing the two GPS stations of the island, for the ascending pass are 19 mm (5
587 mm for the LOS. of the descending pass), and in terms of percentage the postseismic LOS
588 motion is about 15-34 % of the co-seismic one. Our observations support almost one whole
589 fringe on the north coast of the island (ending northern than SAMO), however the same
590 area has been partially subjected to gravitational motions (see Fig. 12 and Fig. 13) so at this
591 stage we didn't proceed further into differentiating those signals. Moreover, the
592 deformation mapped in post-seismic interferograms (secondary images on 11, 17 and 23
593 November 2020), demonstrate the continuation of the post-seismic process, in agreement
594 with the GPS data (Fig. 13). These post-seismic interferograms are stored in the AIPS (see
595 text S2 and http://aips-p.space.noa.gr/Samos/products/131/post).

596 In terms of vertical motions, we also observe a fast postseismic uplift in the data of footwall
597 stations SAMO (Fig. S3) and SAMU. The postseismic uplift ranges between 12-28% of the

co-seismic value measured at the GNSS stations (Table 4) that are located about 3.7 km south of the top-fault line surface projection (Fig. 15). As already mentioned this deformation is due to fault afterslip, so it will be sustained over months or years (Ergintav et al. 2009; Briole et al. 2021) because of the size of the earthquake (M_w=7.0). We also note that the vertical postseismic motion is on the same direction as the co-seismic motion (Fig. 15), i.e., positive thus signifying further uplift of the footwall. We suggest that postseismic uplift is a process that should be included in long-term deformation studies in both fore-arc (e.g., Crete; Robertson et al. 2019; Ott et al. 2021) and back settings (e.g., Corinth; Houghton et al. 2003; Fernandez-Blanco et al. 2020).

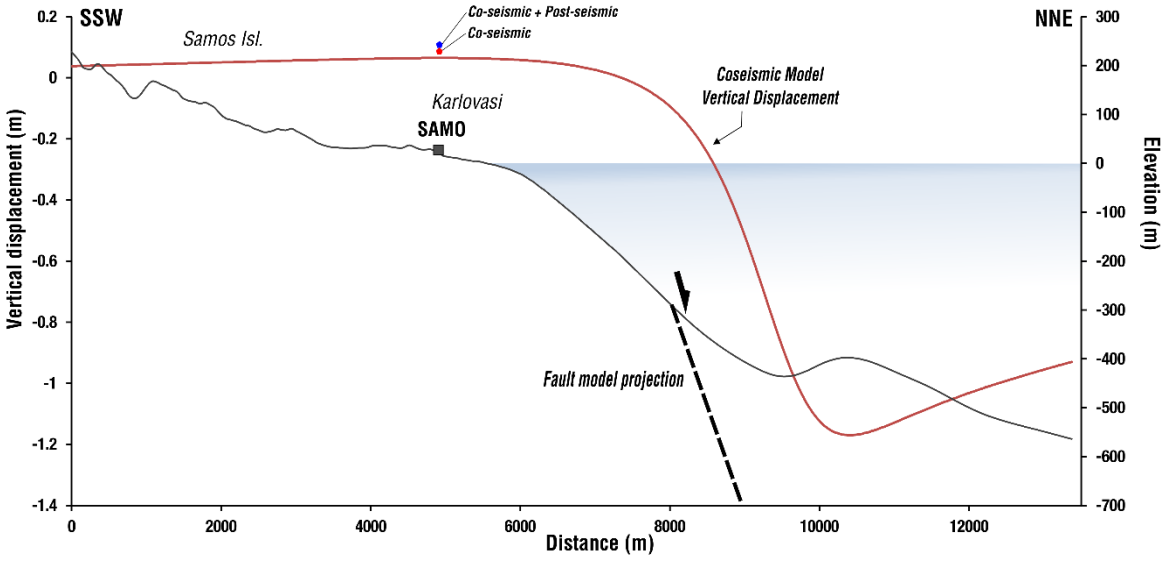

Fig. 15. Cross-section across the seismic fault showing vertical displacement (according to the model of Table 3; red line). GNSS station SAMO is shown on the footwall. The vertical displacement (in m) is shown on the left-Y axis. Elevation and bathymetry are shown on the right-Y axis. Vertical exaggeration is times 6 the horizontal (X-axis).

7.2 Asymmetric Elastic response of the crust

Geodetic processing of GNSS observations can supply reliable and unsaturated measurements of ground motion displacement during earthquakes (e.g., Melgar et al. 2015; Huang et al. 2017; Ruhl et al. 2019). The displacement data are extremely useful for earthquakes with moment magnitudes larger than M=5.0 and originating from stations at the near-field (equal to or less than one fault length) up to regional distances (200-300 km or even more). The displacements comprise measurements (offsets) of GNSS antenna positions due to tectonic strain of the crust imposed by the passage of seismic waves. The peak ground displacements (PGD) are defined on the horizontal plane (sum of offsets of the North-South and East-West component of GNSS; e.g., Ganas et al. 2018) and/or all

three directions of motion (3D; Melgar et al. 2015). The PGDs are related to earthquake magnitude (M_w) and distance to hypocentre R by a relation of the form LOG(PGD) = a + b * Mw + c* LOGR * Mw (Ganas et al. 2018). The Samos event data (Table 2) show that GNSS horizontal displacements increase closer to the epicentre in a systematic way, in agreement with the response of an elastic body to tectonic strain (Fig. 6; Fig. 16). First, we observe that GNSS offset data from "near-field" stations (one fault length) SAMO, SAMU, 093A, (Fig. 6) are in agreement with the PGD scaling relationships where offset data are correlated to earthquake magnitude and distance to hypocentre (Melgar et al. 2015; Ganas et al. 2018b; Ruhl et al. 2019). As with other shallow earthquakes in the Aegean (period of data 1997-2017; Ganas et al. 2018) we mapped a linear displacement field (in Log-Log space) as expected from an elastic response of the crust to the permanent strain caused by instantaneous seismic slip along the offshore fault. However, the stations located across strike (blue squares in Fig. 16) align close to the M_w=7.0 regression line (in agreement with seismology estimates) while the stations located along strike (±45°; red squares) are aligned close to the M_w=6.5 regression line. We attribute this difference in magnitude scaling with distance to the azimuthal position of the GNSS station with respect to the strike of the rupture plane. The pattern of tectonic strain is asymmetric in elastic earth (see the Okada-type model of Fig. S5) and this is reflected on the co-seismic geodetic data (horizontal GNSS offsets). Moreover, there are two stations onshore Ikaria island (IKAR & IKAU; Fig. 6) that are located to the SW of the rupture at a distance of ~60 km from the hypocentre. Those stations scale with the M_w=7.0 regression line despite their azimuthal position (~45° off-strike); we believe that their offsets are impacted by a possible (westward) directivity effect of the rupture. In case of a bilateral rupture, we would anticipate lower PGD at IKAU & IKAR and higher PGD in SAMU, DIDI and ADY1, as the latter three stations are located towards east of the epicentre. The Samos case demonstrates that (when available) GNSS stations across strike of dip-slip ruptures should be considered first in magnitude-scaling estimates. .

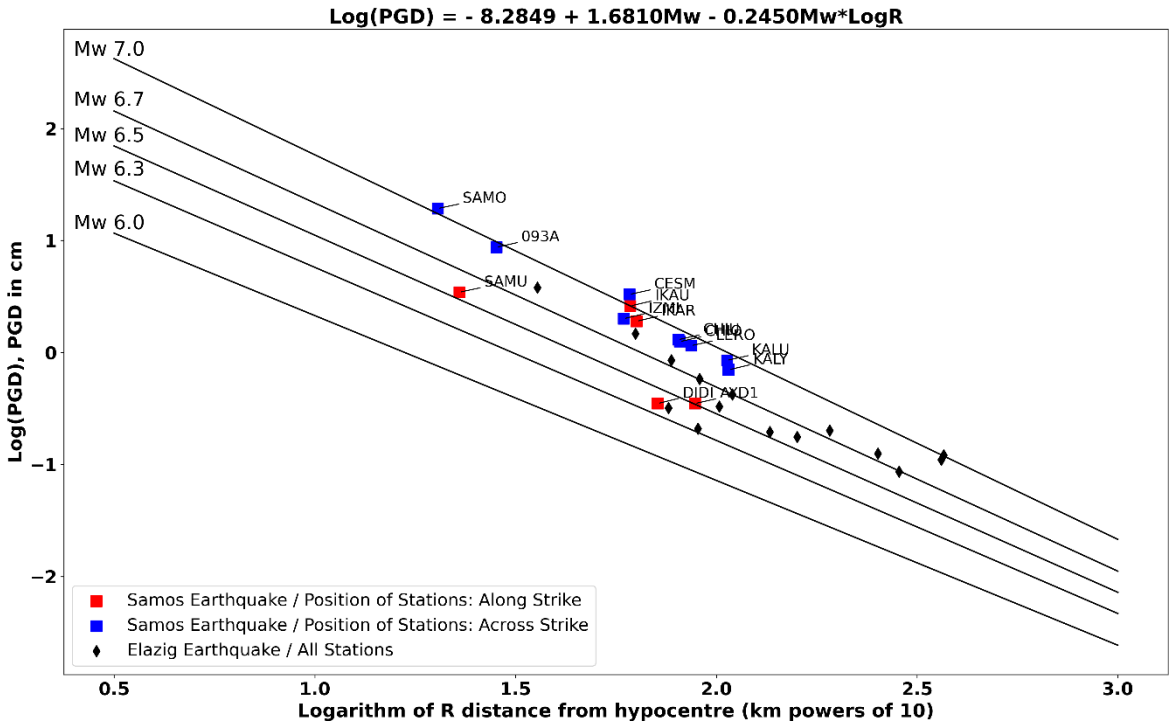

653

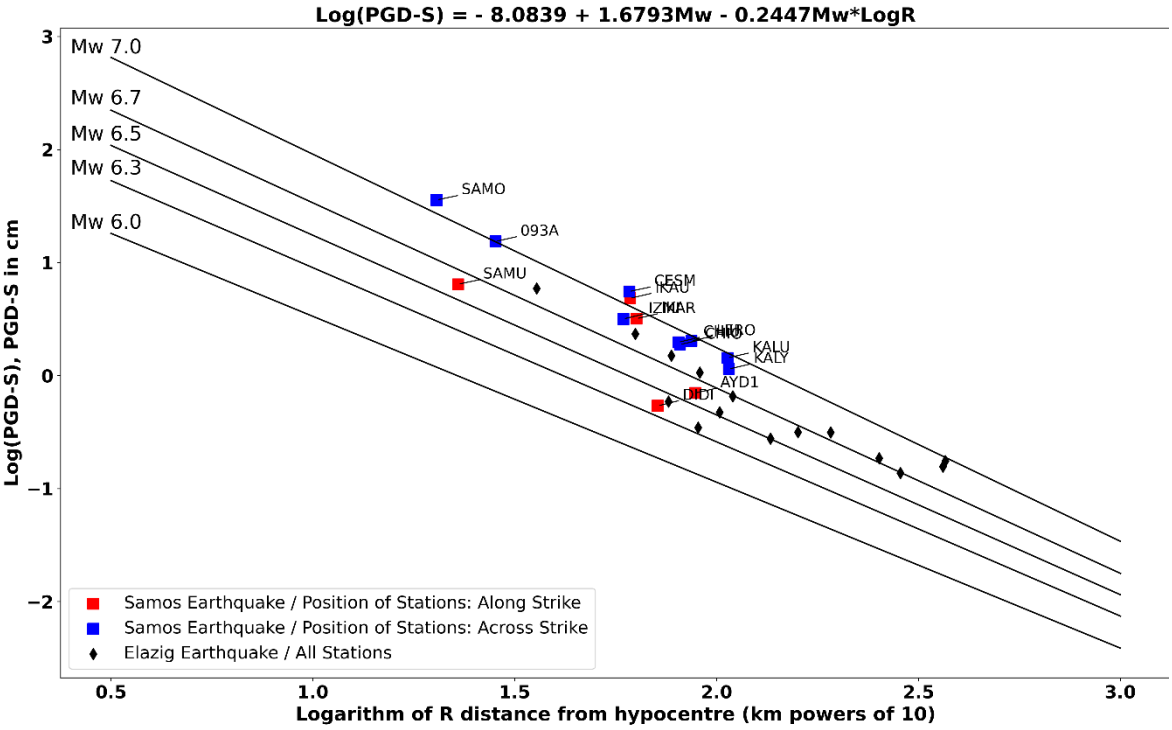

654

655 **Fig. 16:** (top panel) two-dimensional graph of geodetic data (Y-axis; cm) that uses
656 logarithmic scales to show a linear decrease of PGD (peak ground displacement) with
657 hypocentral distance (X-axis; km) for the Elazig (black rhombs) and Samos (coloured
658 squares) earthquakes2020). Blue squares show the Samos earthquake data from GNSS
659 stations across strike. Red stars indicate the data from GNSS stations along strike. Date
660 format in legend (upper right) is YYYYMMDD. (bottom panel) Graph as above but showing
661 decrease of PGD-S (cm) with hypocentral distance (km). The oblique blue lines are the

predicted scaling values for a particular earthquake magnitude from the relations above each graph (from Ganas et al. 2018). The Elazig earthquake data (24 Jan. 2020; M_w=6.7) are from Melgar et al. (2020).

7.3 Extension across the Samos – Kuşadası Bay

In the eastern Aegean crustal extension is accommodated by a combination of normal-slip and strike-slip faulting as demonstrated by geological, seismological and geodetic data (i.e., Boronkay and Doutsos, 1994; Ocakoglou et al. 2004; Benetatos et al. 2006; Ozkaymak and Sozbilir, 2012; Chatzipetros et al. 2013; Tan et al. 2014; Yolsal-Çevikbilen et al. 2014; Ganas et al. 2019), however, in the offshore area of Samos detailed knowledge was lacking. According to our joint-inversion (GNSS & InSAR) model, the main structure is the 40-km long seismic fault (activated by the Samos 2020 earthquake) that dips towards north at an angle of 37° and reaches the depth of 10 – 11 km (Fig. 17). The root of the fault is at the base of the upper crust which comprises about 40-50% of the total crustal thickness (about 30-km thick in the area of Samos; Grigoriadis et al. 2016). As such this fault comprises a major Quaternary structure of the Aegean Sea given that fault length is about 3.3 times the seismogenic part of the crust. It seems that fault growth was more efficient along strike of the fault, although this is not reflected in sea-bottom morphology (that deepens towards the western part of the footwall), similarly to the 1949 earthquake offshore Chios (Melis et al. 2020) and the 2019 earthquake offshore Kos (Ganas et al. 2019).

The Samos fault throw assuming a) pure normal slip and b) flat pre-rift topography, should exceed 2 km (by summing footwall relief south of Karlovassi and offshore basin depth), thus providing a preliminary estimate for a mean throw rate of 1 mm/yr or about 1.4 mm/yr mean slip rate. This fault accommodates a significant portion of tectonic strain accumulation in the Samos – Kuşadası Gulf (Fig. 17) where a crustal block boundary has been suggested by Vernant et al (2014) and Briole et al. (2021). Both fault size and geometry indicate that this is a relatively young structure developed during the Quaternary and represents the main source of seismic hazard in this region. We note that our geodetic data inversion is fit by a planar fault (40 by 15 km), although we are well aware that in nature faults are non-planar.

The surface projection of the fault is found near the northern shore of Samos (Fig. 15; Fig. 17), about 1.5-km offshore the port of Karlovassi, assuming a 37° dip-angle. In addition, the N276°E orientation of the fault is roughly similar to that of the active faults and/or seismogenic sources in this area (Chatzipetros et al. 2013; Caputo and Pavlides, 2013; Ganas et al. 2013). All databases contain an offshore north-dipping normal fault that is described as the main seismic source for the Samos Gulf.

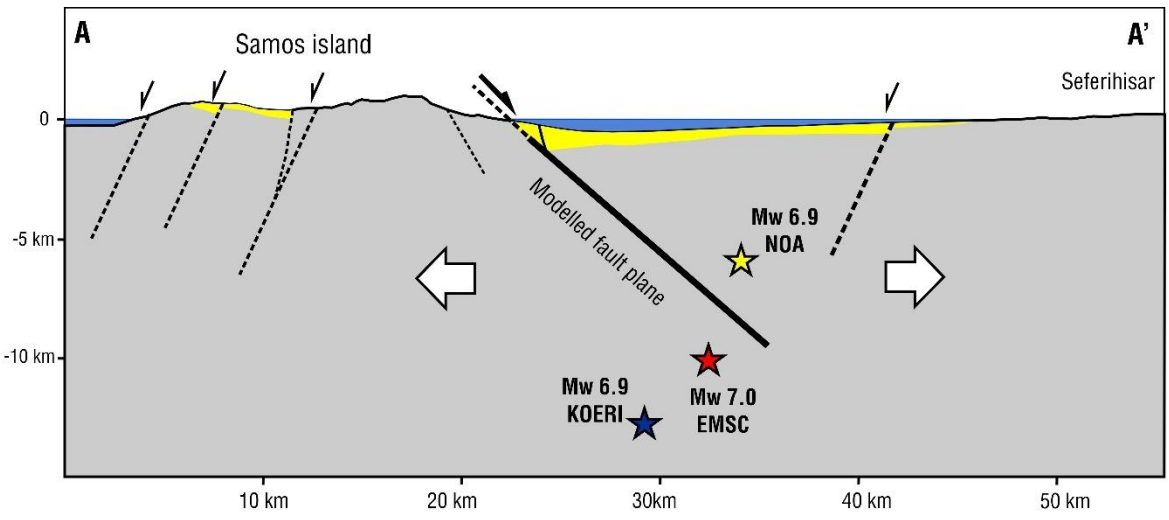

699

700 **Fig. 17.** Tectonic model across the Samos Gulf (See Fig. 1 for location A – A'). Black lines are
701 active faults (half arrow indicates downthrown side). The bold black line corresponds to the
702 model fault, and dashed lines are inferred normal faults from literature. The yellow colour
703 indicates the recent sediment cover. Solid stars indicate mainshock hypocentres, projected
704 onto the cross-section. White solid arrows indicate long-term extensional strain within the
705 crust.

706

707 Although it is crucial for short-term seismic hazard assessment, we cannot infer the
708 structure towards east, i.e., towards the Kuşadası area where large active normal faults
709 exist (Meng et al. 2021). It is possible that the 2020 rupture plane continues eastwards for
710 another 10-15km or that another, north-dipping fault segment exists towards the east of
711 the 2020 rupture. Preliminary aftershock data (Papadimitriou et al. 2020; Foumelis et al.
712 2021) are not conclusive on the geometry of the structure towards east. The eastern cluster
713 of the 2020 aftershocks (offshore NE Samos and onshore eastern Samos; Fig. S1) probably
714 reflects triggered seismicity on optimally-oriented faults to N-S extension because of
715 Coulomb stress transfer (Papadmitriou et al. 2020). More offshore data are needed to
716 better define the fault zone geometry and size, and shed light on a possible co-planar (to
717 2020) configuration of seismic sources or not. Towards the west, the recent offshore
718 seismic survey data by Nomikou et a; (2021), confirm that the Samos earthquake seismic
719 fault has its surface trace roughly projected near the Samos coast (in Fig. 8) following the
720 planar geometry assumed in our inversion. In addition, the main rupture patch extends for
721 ~25-km west of Karlovassi (Fig. 1) as evidenced by the visible E-W gap in the early
722 aftershock (24-hr) distribution. In summary, the proposed fault characteristics (Table 3) as
723 revealed by the 2020 earthquake in terms of location, geometry and seismic potential are
724 robust and they should update the fault databases of active structures of the eastern
725 Aegean Sea (e.g., Papazachos et al., 2001; Ganas et al., 2013; Caputo and Pavlides, 2013;
726 Sakellariou et al., 2013; Emre et al., 2016).

8. Conclusions

1. Our joint inversion (GNSS and InSAR) modeling indicates that the Samos M7.0 earthquake occurred along a north-dipping normal fault. The fault is located offshore Samos occupying a length of 40 km, width of 17 km, an average coseismic slip of 1.7 m, and a moderate dip-angle (37°).
2. The root mean square (r.m.s) error between geodetic data and model is 6.4 mm for the GPS horizontal data, 9.8 mm for the GPS vertical data and between 23 - 59 mm for the InSAR data (see Table 3 for model performance), respectively.
3. The earthquake caused the permanent uplift of the island in the range 1-10 cm with the exception of a coastal strip along part of the northern shore (between Agios Konstantinos – Kokkari) that subsided 2-6 cm.
4. We observed a fast postseismic slip (uplift) ranging between 22-33% of the co-seismic slip value. This is primarily due to fault shallow afterslip as it is recorded within the first 10-days since the mainshock. Postseismic uplift is an important process that should be included in earthquake deformation studies.
5. The effects of the earthquake included liquefaction, rock falls, rock slides, road cracks and deep-seated landslides, all due to the strong ground motion and associated down-slope mobilization of soil cover and loose sediments.
6. The Samos earthquake demonstrates that (when available) GNSS station data (offsets) across strike of dip-slip ruptures should be considered first in magnitude-scaling estimates.

Acknowledgements: We thank Brendan Crowell, Nicolas Chamot-Rooke, Ross Stein, Marco Meschis, Tuncay Taymaz, Diego Melgar, George Papathanassiou, Evi Nomikou, Isidoros Kampolis, Ioannis Kassaras, Antonio Avallone, Eirini Efstathiou, Thekla Thoma and Efthimios Lekkas for comments and discussions. Sentinel-1 and Sentinel-2 satellite imagery was acquired through European Space Agency and Copernicus, and WorldView imagery through Maxar Open Data program. We are indebted to ESA, Geohazards Lab and Terradue for providing access to Geohazards Exploitation Platform (GEP) for InSAR cloud processing. GNSS data were provided by Ktimatologio SA, Hexagon SmartNET and Uranus (Tree) networks of Greece. We thank Tuncay Taymaz and Semi Ergintav for sharing Turkish GNSS data. We thank the Samos local authorities for their help. Several figures were created by use of GMT (Wessel et al. 2019).

Conflict of interest: The authors declare no conflict of interest

References

Angelier J. 1979. Néotectonique de l' arc Egéen. Soc. Géol. Nord, 3, pp. 1-417.

Atzori, S., M. Manunta, G. Fornaro, A. Ganas, S. Salvi, 2008. Postseismic displacement of the 1999 Athens earthquake retrieved by the Differential Interferometry by Synthetic Aperture Radar time series, Journal of Geophysical Research, 113, B09309, doi:10.1029/2007JB005504

Benetatos, C., A. Kiratzi, A. Ganas, M. Ziazia, A. Plessa, and G. Drakatos 2006. Strike-slip motions in the Gulf of Siğaçik (western Turkey): Properties of the 17 October 2005 earthquake seismic sequence, Tectonophysics 426, 3-4, 263-279, DOI: 10.1016/j.tecto.2006.08.003.

Boronkay, K. and Doutsos, T. 1994. Transpression and transtension within different structural levels in the central Aegean region. Journal of Structural Geology, 16 (11), 1555-1573, https://doi.org/10.1016/0191-8141(94)90033-7

Briole, P., 2017. Modelling of earthquake slip by inversion of GNSS and InSAR data assuming homogeneous elastic medium, Zenodo. http://doi.org/10.5281/zenodo.1098399

Briole, P., A. Ganas, P. Elias, D. Dimitrov, 2021. The GPS velocity field of the Aegean. New observations, contribution of the earthquakes, crustal blocks model, Geophysical Journal International, ggab089, https://doi.org/10.1093/gji/ggab089

Caputo, R. S. Pavlides, 2013. The Greek Database of Seismogenic Sources (GreDaSS), version 2.0.0: A compilation of potential seismogenic sources (Mw>5.5) in the Aegean Region. DOI:10.15160/UNIFE/GREDASS/0200.

Cetin, K. O., Mylonakis, G., Sextos, A. Stewart, J. P. Seismological and engineering effects of the Mw 7.0 Samos Island (Aegean Sea) Earthquake, 2020. Hellenic Association of Earthquake Engineering. Report 2020/02. https:// doi. org/ 10. 18118/ G6H088.

Chatzipetros, A., Kiratzi, A., Sboras, S., Zouros, N., Pavlides, S., 2013. Active faulting in the north-eastern Aegean Sea Islands. Tectonophysics, 597-598, pp. 106-122.

Cheloni, D. R. Giuliani, E. D'Anastasio, S. Atzori, R.J. Walters, L. Bonci, N. D'Agostino, M. Mattone, S. Calcaterra, P. Gambino, F. Deninno, R. Maseroli, G. Stefanelli, 2014. Coseismic and post-seismic slip of the 2009 L'Aquila (central Italy) MW 6.3 earthquake and implications for seismic potential along the Campotosto fault from joint inversion of high-precision levelling, InSAR and GPS data. Tectonophysics, 622, 168-185, https://doi.org/10.1016/j.tecto.2014.03.009 .

Chiaraluce, L., Valoroso, L., Piccinini, D., Di Stefano, R., and De Gori, P. 2011. The anatomy of the 2009 L'Aquila normal fault system (central Italy) imaged by high resolution foreshock and aftershock locations, J. Geophys. Res., 116, B12311, doi:10.1029/2011JB008352.

D'Agostino, N., M. Métois, R. Koci, L. Duni, N. Kuka, A. Ganas, I. Georgiev, F. Jouanne, N. Kaludjerovic, R. Kandić, 2020. Active crustal deformation and rotations in the southwestern Balkans from continuous GPS measurements. Earth and Planetary Science Letters, 539, 116246, https://doi.org/10.1016/j.epsl.2020.116246

Ergintav, S., McClusky, S., Hearn, E., Reilinger, R., Cakmak, R., Herring, T., Ozener, H., Lenk, O., and Tari, E. 2009. Seven years of postseismic deformation following the 1999, M = 7.4 and M = 7.2, Izmit-Düzce, Turkey earthquake sequence, J. Geophys. Res., 114, B07403, doi:10.1029/2008JB006021

Evelpidou, N., Karkani, A., Kampolis, I. 2021. Relative Sea Level Changes and Morphotectonic Implications Triggered by the Samos Earthquake of 30th October 2020. J. Mar. Sci. Eng., 9, 40. http://doi.org/10.3390/jmse9010040

Fernández-Blanco, D., de Gelder, G., Lacassin, R., & Armijo, R. 2020. Geometry of flexural uplift by continental rifting in Corinth, Greece. Tectonics, 39, e2019TC005685. https://doi.org/10.1029/2019TC005685

Foumelis, M., Papazachos, C., Papadimitriou, E. et al. 2021. On rapid multidisciplinary response aspects for Samos 2020 M7.0 earthquake. Acta Geophys.. https://doi.org/10.1007/s11600-021-00578-6

Ganas, A., G. Drakatos, S. B. Pavlides, G. N. Stavrakakis, M. Ziazia, E. Sokos, and V. K. Karastathis, 2005. The 2001 Mw = 6.4 Skyros earthquake, conjugate strike-slip faulting and spatial variation in stress within the central Aegean Sea, J. Geodyn., 39(1), 61 – 77, doi:10.1016/j.jog.2004.09.001.

Ganas, A., Drakatos, G., Rontogianni, S., Tsimi, C., Petrou, P., Papanikolaou, M., Argyrakis, P., Boukouras, K., Melis, N., Stavrakakis, G. 2008. NOANET: the new permanent GPS network for Geodynamics in Greece. European Geophysical Union, Geophysical Research Abstracts 10, EGU2008-A-04380.

Ganas, A., Parsons, T., 2009. Three-dimensional model of Hellenic Arc deformation and origin of the Cretan uplift. J. Geophys. Res.: Solid Earth 114 (B6) https://doi.org/10.1029/2008JB005599 .

Ganas, A., Oikonomou, A. and Tsimi, Chr, 2013. NOAfaults: a digital database for active faults in Greece. Bulletin Geological Soc. Greece, 47, 518-530, http://dx.doi.org/10.12681/bgsg.11079

Ganas, A., Elias, P., Kapetanidis, V, Valkaniotis, S., Briole, P., Kassaras, I., Argyrakis, P., Barberopoulou, A., Moshou, A., 2019. The July 20, 2017 M6.6 Kos Earthquake: Seismic and Geodetic Evidence for an Active North-Dipping Normal Fault at the Western End of the Gulf of Gökova (SE Aegean Sea), Pure and Applied Geophysics, 176 (10), 4177-4211 https://doi.org/10.1007/s00024-019-02154-y

Ganas, A., Elias, P., Briole, P., Tsironi, V., Valkaniotis, S., Escartin, J., Karasante, I., and Efstathiou, E., 2020a, Fault responsible for Samos earthquake identified, Temblor, http://doi.org/10.32858/temblor.134

Ganas A, Briole P, Bozionelos G, Barberopoulou A, Elias P, Tsironi V, Valkaniotis S, Moshou A, Mintourakis I, 2020b. The 25 October 2018 Mw= 6.7 Zakynthos earthquake (Ionian Sea, Greece): a low-angle fault model based on GNSS data, relocated seismicity, small tsunami and implications for the seismic hazard in the west Hellenic Arc, Journal of Geodynamics doi: https://doi.org/10.1016/j.jog.2020.101731

Ganas, A., Elias, P., Briole, P., Cannavo, F., Valkaniotis, S., Tsironi, V., Partheniou, E.I. 2020c. Ground Deformation and Seismic Fault Model of the M6.4 Durres (Albania) Nov. 26, 2019 Earthquake, Based on GNSS/INSAR Observations. Geosciences, 10 (6), 210 https://www.mdpi.com/2076-3263/10/6/210/htm

Goldstein, R. M.; Werner, C. L. 1998. Radar interferogram filtering for geophysical applications. Geophys. Res. Lett. 25(21), 4035-4038.

Grigoriadis, V.N., Tziavos, I.N., Tsokas, G.N. et al. 2016. Gravity data inversion for Moho depth modeling in the Hellenic area. Pure Appl. Geophys. 173, 1223–1241. https://doi.org/10.1007/s00024-015-1174-y

Houghton, S. L., G. P. Roberts, I. D. Papanikolaou, J. M. McArthur, and M. A. Gilmour, 2003. New 234U-230Th coral dates from the western Gulf of Corinth: Implications for extensional tectonics, Geophys. Res. Lett., 30(19), 2013, doi:10.1029/2003GL018112.

Huang, Y., Yang S., Qiao, X., Lin, M., Zhao, B., Tan, K. 2017. Measuring ground deformations caused by 2015 Mw7.8 Nepal earthquake using high-rate GPS data, Geodesy and Geodynamics, 8, 4, pp. 285-291, https://doi.org/10.1016/j.geog.2017.03.003

Institute of Engineering Seismology and Earthquake Engineering, 2020. Earthquake North of Samos Island (Greece) of 30/10/2020, Preliminary Report, Thessaloniki.

Kalogeras I, Melis NS, Kalligeris N 2020. The earthquake of October 30th, 2020 at Samos, Eastern Aegean Sea, Greece. Preliminary Report, National Observatory of Athens, Institute of Geodynamics. https://accelnet.gein.noa.gr/ 2020/ 11/ 09/the- earthquake- of-october-30th- 2020- at- samos- eastern- aegean- sea- greece- preliminary- report Lacroix, P., Perfettini, H., Taipe, E. and Guillier, B., 2014. Coseismic and postseismic motion of a landslide: Observations, modeling, and analogy with tectonic faults. Geophys. Res. Lett. 41, 6676–6680 http://doi.org/10.1002/2014GL061170

Lacroix, P., Handwerger, A.L. and Bièvre, G., 2020. Life and death of slow-moving landslides. Nat. Rev. Earth. Environ., 1, 404–419. https://doi.org/10.1038/s43017-020-0072-8

869 Lekkas, E., Mavroulis, S., Gogou, GA, et al 2020. The October 30, 2020, Mw 6.9 Samos
870 (Greece) earthquake. Newsletter of Environmental, Disaster and Crises Management
871 Strategies, 21, ISSN 2653-9454, Athens, Greece.

872 Mascle, Jean, and Laure Martin, 1990. Shallow structure and recent evolution of the
873 Aegean Sea: A synthesis based on continuous reflection profiles, Marine Geology, Volume
874 94, Issue 4, Pages 271-299.

875 Mavroulis, S., Triantafyllou, I., Karavias, A., Gogou, M., Katsetsiadou, K.-N., Lekkas, E.,
876 Papadopoulos, G.A., Parcharidis, I. 2021. Primary and Secondary Environmental Effects
877 Triggered by the 30 October 2020, Mw = 7.0, Samos (Eastern Aegean Sea, Greece)
878 Earthquake Based on Post-Event Field Surveys and InSAR Analysis. Appl. Sci., 11, 3281.
879 https://doi.org/10.3390/app11073281

880 McClusky, S., et al. 2000, Global Positioning System constraints on plate kinematics and
881 dynamics in the eastern Mediterranean and Caucasus, J. Geophys. Res. 105, B3, 5695-5719,
882 http://doi.org/10.1029/1999JB900351

883 McKenzie, D. 1978. Active tectonics of the Alpine–Himalayan belt: the Aegean Sea and
884 surrounding regions, Geophys. J. Roy. Astr. Soc. 55, 1, 217-254,
885 http://doi.org/10.1111/j.1365-246X.1978.tb04759.x .

886 Melgar, D., B. W. Crowell, J. Geng, R. M. Allen, Y. Bock, S. Riquelme, E. M. Hill, M. Protti,
887 and A. Ganas, 2015. Earthquake magnitude calculation without saturation from the scaling
888 of peak ground displacement, Geophys. Res. Lett., 42,
889 http://onlinelibrary.wiley.com/doi/10.1002/2015GL064278/full .

890 Melgar, D., A. Ganas, J. Geng, C. Liang, E. J. Fielding, and I. Kassaras, 2017. Source
891 characteristics of the 2015 Mw6.5 Lefkada, Greece, strike-slip earthquake, J. Geophys. Res.
892 Solid Earth, 122, http://dx.doi.org/10.1002/2016JB013452

893 Melgar, D. A. Ganas, T. Taymaz, S. Valkaniotis, B. W Crowell, V. Kapetanidis, V. Tsironi, S.
894 Yolsal-Çevikbilen, T. Öcalan, 2020. Rupture kinematics of 2020 January 24 Mw 6.7
895 Doğanyol-Sivrice, Turkey earthquake on the East Anatolian Fault Zone imaged by space
896 geodesy, Geophysical Journal International, Volume 223, Issue 2, Pages 862–874,
897 https://doi.org/10.1093/gji/ggaa345

898 Melis, N.S., Okal, E.A., Synolakis, C.E. et al. 2020. The Chios, Greece Earthquake of 23 July
899 1949: Seismological Reassessment and Tsunami Investigations. Pure Appl. Geophys. 177,
900 1295–1313. https://doi.org/10.1007/s00024-019-02410-1

901 Meng, J., Sinoplu, O., Zhou, Z. et al. 2021. Greece and Turkey Shaken by African tectonic
902 retreat. Sci Rep 11, 6486. https://doi.org/10.1038/s41598-021-86063-y

903 Moro, M., M. Chini, M. Saroli, S. Atzori, S. Stramondo, and S. Salvi, 2011. Analysis of large,
904 seismically induced, gravitational deformations imaged by high-resolution COSMO-SkyMed
905 synthetic aperture radar, Geology, 39(6), 527–530, https://doi.org/10.1130/G31748.1

906 Mountrakis, D., Kilias, A., Vavliakis E., Psilovikos, A. Sc Thomaidou, E., 2003. Neotectonic
907 map of Samos island (Aegean Sea, Greece): Implication of geographical information
908 systems in the geological mapping. — Proceedings Volume 1, 4th European Congress on
909 Regional Geoscientific Cartography and Information Systems, 11-13, Bologna, Italy.

910 Neo, JC. Huang, Y. Yao, D. and Wei, S., 2020. Is the Aftershock Zone Area a Good Proxy for
911 the Mainshock Rupture Area?. Bulletin of the Seismological Society of America, 111 (1):
912 424–438. doi: https://doi.org/10.1785/0120190200

913 NOAFAULTs KMZ layer Version 2.1 (2019 update) (Version V2.1) [Data set]. Zenodo.
914 http://doi.org/10.5281/zenodo.3483136

915

916 Nomikou, P., Evangelidis, D., Papanikolaou, D., Lampridou, D., Litsas, D., Tsaparas, Y.,
917 Koliopanos, I. 2021. Morphotectonic Analysis along the Northern Margin of Samos Island,
918 Related to the Seismic Activity of October 2020, Aegean Sea, Greece. Geosciences, 11, 102.
919 https://doi.org/10.3390/geosciences11020102

920 Ocakoglu, N., Demirbag, E. & Kuscu, I. 2004. Neotectonic structures in the area offshore of
921 Alaçatı, Doğanbey and Kuşadası (western Turkey): evidence of strike-slip faulting in the
922 Aegean extensional province. Tectonophysics 391, 67–83.

923 Okada, Y. 1985. Surface deformation due to shear and tensile faults in a half-space. Bull
924 Seismol Soc Am, 75:1135-1154.

925 Okrusch, M., P. Richter and G. Katsikatsos, 1984. High-pressure rocks of Samos, Greece.
926 Geological Society, London, Special Publications, 17, 529-536,
927 https://doi.org/10.1144/GSL.SP.1984.017.01.39

928 Ott, R., Wegmann, K.W., Gallen, S.F., Pazzagila, F.J., Brandon, M., Ueda, K., Fassoulas, C.,
929 2021. Reassessing Eastern Mediterranean tectonics and earthquake hazards from the AD
930 365 earthquake: AGU Advances, in press.

931 Özkaymak, C., and Sözbilir, H., 2012. Tectonic geomorphology of the Spildağı High Ranges,
932 western Anatolia, Geomorphology, 173–174, 128-140.

933 Papadimitriou P., Kapetanidis V., Karakonstantis A., Spingos I., Kassaras I., Sakkas V.,
934 Kouskouna V., Karatzetzou A., Pavlou K., Kaviris G. and Voulgaris N. 2020. First Results on
935 the Mw=6.9 Samos Earthquake of 30 October 2020. Bulletin Geological Society of Greece,
936 56, 251-279 https://doi.org/10.12681/bgsg.25359

Papadopoulos, G. A., Latoussakis, I., Daskalaki, E., Diakogianni, G., Fokaefs, A., Kolligri, M., Liadopoulou, K., Orfanogiannaki, K., and Pirentis, A. 2006. The East Aegean Sea strong earthquake sequence of October–November 2005: lessons learned for earthquake prediction from foreshocks, Nat. Hazards Earth Syst. Sci., 6, 895–901, https://doi.org/10.5194/nhess-6-895-2006.

Papanikolaou D. 1979. Unités tectoniques et phases de déformation dans l'îsle de Samos, Mer Egée, Grèce. Bull. Soc. Géol. France, 21, 745–752.

Papazachos, B. C., Mountrakis, D. M., Papazachos, C. B., Tranos, M. D., Karakaisis, G. F., and Savvaidis, A. S., 2001. The faults which have caused the known major earthquakes in Greece and surrounding region between the 5th century BC and today. In Proceedings of 2nd National Conference Anti-Seismic Engineering and Technical Seismology, 17–26, Technical Chamber of Greece, Thessaloniki, Greece.

Pousse-Beltran, L., Socquet, A., Benedetti, L., Doin, M.-P., Rizza, M., & D'Agostino, N. 2020. Localized afterslip at geometrical complexities revealed by InSAR after the 2016 Central Italy seismic sequence. Journal of Geophysical Research: Solid Earth, 125, e2019JB019065. https://doi.org/10.1029/2019JB019065

Reilinger, R. S. McClusky, D. Paradissis, S. Ergintav, P. Vernant, 2010. Geodetic constraints on the tectonic evolution of the Aegean region and strain accumulation along the Hellenic subduction zone, Tectonophysics, Volume 488, Issues 1–4, Pages 22-30, https://doi.org/10.1016/j.tecto.2009.05.027.

Ring, U., S. Laws, M. Bernet, 1999. Structural analysis of a complex nappe sequence and late-orogenic basins from the Aegean Island of Samos, Greece, Journal of Structural Geology, 21, 11, 1575-1601, https://doi.org/10.1016/S0191-8141(99)00108-X .

Robertson, J., Meschis, M., Roberts, G.P, Ganas A., Gheorgiou, D., 2019. Temporally constant Quaternary uplift rates and their relationship with extensional upper-plate faults in south Crete (Greece), constrained with 36Cl exposure dating. Tectonics. 38 (4), 1189-1222. https://doi.org/10.1029/2018TC005410

Ruhl, CJ., D. Melgar, J. Geng, DE Goldberg, BW Crowell, RM Allen, Y. Bock, S. Barrientos, S. Riquelme, JC Baez, E. Cabral-Cano, X. Pérez-Campos, EM Hill, M. Protti, A. Ganas, M. Ruiz, P. Mothes, P. Jarrín, JM Nocquet, JP Avouac, E. D'Anastasio, 2019. A Global Database of Strong-Motion Displacement GNSS Recordings and an Example Application to PGD Scaling, Seismological Research Letters, 90 (1), 271-279 https://doi.org/10.1785/0220180177

Sakellariou, D., Mascle, J., & Lykousis, V. 2013. Strike slip tectonics and transtensional deformation in the Aegean region and the Hellenic arc: Preliminary results. Bulletin of the Geological Society of Greece, 47, 647-656 http://dx.doi.org/10.12681/bgsg.11098

Stiros, S.C., J. Laborel, F. Laborel-Deguen, S. Papageorgiou, J. Evin, P.A. Pirazzoli, 2000. Seismic coastal uplift in a region of subsidence: Holocene raised shorelines of Samos Island, Aegean Sea, Greece, Marine Geology, Volume 170, Issues 1–2, 41-58, https://doi.org/10.1016/S0025-3227(00)00064-5 .

Tan, O., Papadimitriou, E.E., Pabucçu, Z. et al. 2014. A detailed analysis of microseismicity in Samos and Kusadasi (Eastern Aegean Sea) areas. Acta Geophys. 62, 1283–1309. https://doi.org/10.2478/s11600-013-0194-1

Taymaz, T., J. Jackson, and D. McKenzie 1991. Active tectonics of the north and central Aegean Sea, Geophys. J. Int. 106, 2, 433-490, DOI: 10.1111/j.1365-246X.1991.tb03906.x

Theodoropoulos, D. 1979. Geological Map of Greece, 1:50,000 scale; Neon Karlovasi and Limin Vatheos Sheets. IGME, Athens, Greece.

Triantafyllou, I.; Gogou, M.; Mavroulis, S.; Lekkas, E.; Papadopoulos, G.A.; Thravalos, M. 2021. The Tsunami Caused by the 30 October 2020 Samos (Aegean Sea) Mw7.0 Earthquake: Hydrodynamic Features, Source Properties and Impact Assessment from Post-Event Field Survey and Video Records. J. Mar. Sci. Eng. 9, 68. https://doi.org/10.3390/jmse9010068
Vadaloukas, G., Vintzileou, E., Ganas, A., Giarlelis, C., Ziotopoulou, K., Theodoulidis, N., Karasante, I., Margaris, B., Mylonakis, G., Papachristidis, A., Repapis, C., Psarropoulos, P. N., & Sextos, A. G. 2020. Samos Earthquake of 30th October, 2020. Preliminary Report of the Hellenic Association for Earthquake Engineering, Athens, Greece. https://doi.org/10.13140/RG.2.2.22609.76644

Vernant, Philippe; Robert Reilinger, Simon McClusky, 2014. Geodetic evidence for low coupling on the Hellenic subduction plate interface, Earth and Planetary Science Letters, Volume 385, Pages 122-129, https://doi.org/10.1016/j.epsl.2013.10.018 .

Wessel, P., Luis, J. F., Uieda, L., Scharroo, R., Wobbe, F., Smith, W. H. F., & Tian, D. 2019. The Generic Mapping Tools version 6. Geochemistry, Geophysics, Geosystems, 20, 5556–5564.

Yolsal-Çevikbilen, S., Taymaz, T., and Helvacı, C. 2014. Earthquake mechanisms in the Gulfs of Gökova, Sığacık, Kuşadası, and the Simav Region (western Turkey): Neotectonics, seismotectonics and geodynamic implications, Tectonophysics, 635, 100-124, https://doi.org/10.1016/j.tecto.2014.05.001.

Supplementary material

Text S1.

AFAD	https://deprem.afad.gov.tr/downloadDocument?id=2064
GFZ	http://geofon.gfz-potsdam.de/eqinfo/event.php?id=gfz2020vimx
GCMT	https://www.globalcmt.org/CMTsearch.html
INGV	http://autorcmt.bo.ingv.it/quicks.html
IPGP	http://geoscope.ipgp.fr/index.php/en/catalog/earthquake-description?seis=us7000c7y0
KOERI	http://udim.koeri.boun.edu.tr/zeqmap/osmapen.asp
UOA	http://www.geophysics.geol.uoa.gr/stations/gmaps3/eventpage_leaf.php?scid=nkua2020vimx&lng=en
NOA	http://bbnet.gein.noa.gr/HL/seismicity/mts/revised-moment-tensors
OCA	http://sismoazur.oca.eu/focal_mechanism_emsc?start=2020-10-29&end=2020-10-31&minlat=0.00&minlon=0.00&maxlat=38.00&maxlon=27.00&mindepth=0&maxdepth=20&minmag=5&maxmag=7.5&eventtype=all
USGS	https://earthquake.usgs.gov/earthquakes/eventpage/us7000c7y0/executive

Text S2:

AIPS (http://aips.space.noa.gr) is a platform for routine (updated in every new acquisition) and on-demand SENTINEL-1 interferogram processing service. It provides freely the original, the filtered, using the adaptive power spectrum filter of Goldstein and Werner (1998) with a coherence threshold of 0.3, interferograms as well as its amplitude in UTM/WGS Transverse Mercator projection, at full resolution (25 m), in GEOTIFF format. It is based on ESA's SNAP (http://step.esa.int/main/) software version 6.0. The multiblock factor is 6 in range and 2 in azimuth. Moreover, it produces figures and raw images in PNG format as quick-look products. The digital elevation model (DEM) used for the processing is the Shuttle Radar Topography Mission (SRTM) 1 Arc-Second Global (doi number: /10.5066/F7PR7TFT). During the stage of processing, the interferogram was formed by cross-multiplying the post-event acquisition image) with the complex conjugate of the pre-event image). The resulting phase represents the difference between the two images. Currently the routine processing includes four tracks of central Greece and one-track form Etna in Sicily, Italy but there is the flexibility to extend the processing upon request. It keeps a rolling-archive with old data stored offline. The on-demand service is triggered upon a moderate or big earthquake in the Euro-Mediterranean region. For the case of the Samos earthquake the interferometric products can be found at http://aips-p.space.noa.gr/Samos/products/

Table S1.

List of the pre-seismic, co-seismic and post-seismic interferograms of the track 131, 29 and 36, produced by AIPS and stored at http://aips-p.space.noa.gr/Samos/products/. The interferograms in bold and framed are used to produce the average interferograms of track 29 and 36 that were used in the inversion modelling.

Ascending track 131			Ascending track 29		Descending track 36		
pre-seismic	co-seismic	post-seismic	co-seismic	post-seismic	pre-seismic	co-seismic	post-seismic
20201018-20201024	20201018-20201111 20201024-20201030 20201018-20201030 20201024-20201123 20201018-20201105 20201018-20201117 20201006-20201111 20201024-20201117 20201018-20201123 20201012-20201030 20201024-20201111 20201006-20201105 20201024-20201105 20201012-20201117 20201006-20201030 20201012-20201111 20201012-20201105	20201117-20201123 20201030-20201105 20201105-20201123 20201030-20201117 20201030-20201123 20201111-20201117 20201111-20201123 20201030-20201111 20201105-20201111 20201105-20201117	20201017-20201104 **20201023-20201116** 20201029-20201122 **20201023-20201110** **20201011-20201110** 20201029-20201104 20201023-20201122 20201017-20201110 20201011-20201104 20201029-20201116 20201023-20201104 20201017-20201116 **20201011-20201116** 20201029-20201110 20201017-20201122	20201110-20201116 20201104-20201110 20201110-20201122 20201116-20201122 20201104-20201116 20201104-20201122	20201024-20201030	**20201024-20201111** **20201006-20201111** 20201030-20201111 **20201024-20201117** 20201006-20201105 20201018-20201105 20201012-20201117 20201012-20201105 20201018-20201123 20201018-20201117 20201030-20201105 20201030-20201123 20201030-20201117 20201024-20201117 20201024-20201123 **20201024-20201123** 20201018-20201111	20201111-20201123 20201105-20201123 20201105-20201117 20201111-20201117 20201105-20201111 20201117-20201123

Table S2. List of GNSS displacement data (mm; E, N, Up components) and their uncertainties.

				dE	dN	dU	sE	sN	sU
coseismic	**SAMO**	26.7053	37.7927	-30	-356	82	2	2	4
	SAMU	26.9734	37.7575	-5	-64	21	2	2	4
	093A	26.8334	37.6716	22	-152	23	3	3	6
	CHIO	26.1272	38.3679	-8	17	2	3	3	6
	CHIU	26.136	38.3665	-8	18	5	2	2	4
	IKAR	26.2243	37.6282	-7	-31	7	3	3	6
	IKAU	26.2733	37.6055	-4	-48	4	3	3	6
	KALU	26.9617	36.9624	3	-14	-3	2	2	4
	LERO	26.8545	37.1364	3	-20	-	2	2	-
	KALY	26.9762	36.9558	3	-11	-1	3	3	6
	AYD1	27.8378	37.8407	0	7	-	8	8	-
	CESM	26.3726	38.3038	-12	54	-	8	8	-
	IZMI	27.0819	38.3948	10	30	2	2	2	4
	DIDI	27.2687	37.3721	2	-5	-	8	8	-
Coseismic + 10 days posteismic	**SAMO**	26.7053	37.7927	-41	-400	100	2	2	4
	SAMU	26.9734	37.7575	-5	-80	28	2	2	4
	CHIO	26.1272	38.3679	-8	22	2	3	3	6
	CHIU	26.136	38.3665	-10	23	5	2	2	4
	IKAR	26.2243	37.6282	-5	-41	7	3	3	6
	IKAU	26.2733	37.6055	-14	-50	4	3	3	6
	KALU	26.9617	36.9624	3	-14	-3	2	2	4
	LERO	26.8545	37.1364	3	-11	-	2	2	-
	KALY	26.9762	36.9558	3	-23	-1	3	3	6
	AYD1	27.8378	37.8407	0	7	-	8	8	-
	CESM	26.3726	38.3038	-12	54	-	8	8	-
	IZMI	27.0819	38.3948	12	36	2	2	2	4
	DIDI	27.2687	37.3721	2	-5		8	8	

Table S3.

List of the picked LOS values from the averaged interferograms. The deformation direction for the LOS. is at the notion of pre-event minus post-event, thus values increasing towards satellite. Lon: Longitude (°), lat is latitude (°). InSAR and modelled values are in mm. The picks are displayed in **Fig. S6**.

	ASCENDING track 29				DESCENDING track 36			
Pick No	**lon**	**lat**	**InSAR**	**model**	**lon**	**lat**	**InSAR**	**model**
1	26.644	37.772	114	112.6	26.761	37.678	28	31.6
2	26.668	37.769	114	110.7	26.800	37.688	28	38.7
3	26.695	37.768	114	111.3	26.825	37.695	28	43.1
4	26.717	37.769	114	112.8	26.852	37.706	28	48.8
5	26.735	37.775	114	118.5	26.868	37.722	28	55.5
6	26.745	37.784	114	128.7	26.861	37.752	28	68.5
7	26.751	37.796	114	134.9	26.842	37.766	28	72.4
8	26.746	37.808	114	108.5	26.826	37.777	28	75.0
9	26.740	37.812	114	69.7	26.813	37.791	28	75.7
10	26.651	37.705	86	63.6	26.798	37.806	28	39.6
11	26.668	37.716	86	69.3	26.807	37.806	0	35.9
12	26.690	37.728	86	76.0	26.818	37.796	0	69.6
13	26.713	37.738	86	82.4	26.865	37.776	0	75.6
14	26.736	37.748	86	90.2	26.882	37.771	0	74.5
15	26.751	37.757	86	98.0	26.902	37.768	0	68.3
16	26.766	37.766	86	106.9	26.586	37.748	28	36.3
17	26.776	37.776	86	119.4	26.621	37.728	28	31.4
18	26.777	37.790	86	132.7	26.642	37.700	28	23.6
19	26.775	37.801	86	127.3	26.841	37.783	0	75.1
20	26.762	37.809	86	93.7	26.977	37.766	0	29.2
21	26.755	37.811	86	71.8	26.992	37.758	0	27.7
22	26.758	37.691	58	46.0	27.006	37.754	0	25.6
23	26.778	37.699	58	46.9	27.026	37.749	0	22.4
24	26.797	37.707	58	47.3	26.815	37.808	-28	-5.4
25	26.815	37.715	58	48.2	26.833	37.795	-28	66.5
26	26.834	37.723	58	47.9	26.851	37.787	-28	72.6
27	26.852	37.731	58	47.5	26.871	37.786	-28	71.7
28	26.863	37.742	58	50.9	26.920	37.769	-28	58.5
29	26.863	37.758	58	66.6	27.042	37.746	0	20.2
30	26.849	37.773	58	96.6	26.824	37.805	-56	26.9
31	26.826	37.783	58	119.9	26.839	37.799	-56	54.2
32	26.810	37.790	58	129.7	26.857	37.795	-56	58.3
33	26.797	37.798	58	129.2	26.959	37.772	0	32.6
34	26.784	37.809	58	62.9				
35	26.782	37.659	30	29.2				
36	26.799	37.652	30	24.8				
37	26.810	37.648	30	22.2				

38	26.827	37.647	30	19.5
39	26.851	37.647	30	16.1
40	26.867	37.652	30	14.7
41	26.882	37.659	30	13.9
42	26.965	37.696	30	11.3
43	26.986	37.707	30	12.6
44	26.997	37.717	30	14.3
45	27.000	37.729	30	17.1
46	26.993	37.742	30	21.0
47	26.989	37.758	30	27.2
48	26.980	37.772	30	34.3
49	26.965	37.780	30	41.3
50	26.949	37.782	30	45.1
51	26.875	37.783	30	93.6
52	26.853	37.784	30	111.5
53	26.834	37.790	30	125.5
54	26.822	37.795	30	128.4
55	26.806	37.802	30	113.0
56	26.797	37.809	30	60.1
57	26.860	37.794	2	117.4
58	26.842	37.796	2	121.9
59	26.832	37.799	2	119.8
60	26.821	37.803	2	106.2
61	26.813	37.808	2	52.8
62	26.856	37.802	-26	91.1
63	26.846	37.802	-26	96.9
64	26.834	37.804	-26	84.4

Table S4. List with locations of field surveyed earthquake effects.

Date	LAT	LON	Location	Feature
06-11-20	37.782800	26.952165	NW Vathy	building damage
06-11-20	37.782800	26.952170	NW Vathy	building damage
06-11-20	37.782865	26.951988	NW Vathy	building damage
06-11-20	37.770015	26.967010	Vathy	Landslide
06-11-20	37.753943	26.976883	Vathy	building damage
06-11-20	37.753864	26.976861	Vathy	building damage
06-11-20	37.753657	26.976442	Vathy	cracks
06-11-20	37.753572	26.976501	Vathy	cracks
06-11-20	37.753573	26.976502	Vathy	cracks
06-11-20	37.751111	26.959167	Kokkari	Camp
06-11-20	37.796880	26.857543	Avlakia	Landslide
06-11-20	37.797113	26.857372	Avlakia	Landslide
06-11-20	37.796700	26.857658	Avlakia	Landslide
06-11-20	37.796515	26.857833	Avlakia	Landslide
06-11-20	37.809698	26.791153	Livadaki	road cracks
06-11-20	37.809697	26.791152	Livadaki	road cracks
06-11-20	37.809696	26.791151	Livadaki	road cracks
06-11-20	37.809647	26.790563	Livadaki	road cracks
06-11-20	37.809684	26.791061	Livadaki	road cracks
06-11-20	37.809584	26.790536	Livadaki	road protection blocks
06-11-20	37.792673	26.705121	Karlovasi	School damage
06-11-20	37.792722	26.705295	Karlovasi	GNSS Antenna SAMO
06-11-20	37.792741	26.705278	Karlovasi	GNSS Antenna SAMO
06-11-20	37.792778	26.705278	Karlovasi	GNSS Antenna SAMO
06-11-20	37.790618	26.704542	Karlovasi	Church Theotokou
06-11-20	37.790800	26.704401	Karlovasi	Church Theotokou
06-11-20	37.790339	26.704289	Karlovasi	building damage – yellow mark
06-11-20	37.790438	26.704197	Karlovasi	Church Theotokou
06-11-20	37.790525	26.703200	Karlovasi	Church Theotokou
06-11-20	37.790524	26.703200	Karlovasi	Church Theotokou
06-11-20	37.794683	26.680910	Karlovasi	Port
06-11-20	37.795409	26.678122	Karlovasi	Jetty - view coastline
06-11-20	37.796130	26.678811	Karlovasi	Jetty - corner - crack
06-11-20	37.796130	26.678809	Karlovasi	Jetty - corner
06-11-20	37.796110	26.678809	Karlovasi	Jetty - corner - crack
06-11-20	37.796308	26.678824	Karlovasi	Jetty - centre -crack
06-11-20	37.796308	26.678824	Karlovasi	Jetty - centre - liquefaction
06-11-20	37.796589	26.678989	Karlovasi	Jetty - centre -crack
06-11-20	37.796635	26.678836	Karlovasi	Jetty wall -crack
06-11-20	37.796695	26.678981	Karlovasi	Jetty - corner - pop-up
06-11-20	37.796694	26.678981	Karlovasi	Jetty - corner - pop-up
06-11-20	37.798332	26.682602	Karlovasi	Jetty-crack
06-11-20	37.798235	26.682622	Karlovasi	Jetty-crack
07-11-20	37.750716	26.961429	Vathy	road cracks
07-11-20	37.750719	26.961334	Vathy	road cracks

07-11-20	37.773889	26.897222	Kokkari	collapse
07-11-20	37.778270	26.884915	Kokkari	collapse
07-11-20	37.796413	26.857920	Avlakia	Landslide
07-11-20	37.796610	26.857723	Avlakia	Landslide
07-11-20	37.798812	26.849460	Road to Vourliotes	collapse
07-11-20	37.799737	26.852413	Road to Vourliotes	Fault
07-11-20	37.799925	26.852378	Road to Vourliotes	Fault
07-11-20	37.803827	26.826588	Agios Konstantinos	building damage
07-11-20	37.803861	26.826472	Agios Konstantinos	building damage
07-11-20	37.799722	26.851667	Agios Konstantinos	building damage
07-11-20	37.799722	26.851667		Raised beach
07-11-20	37.799722	26.851667		Raised beach
07-11-20	37.810219	26.771204	Petalides	raised coastline
07-11-20	37.809229	26.743253	Agios Nikolaos	road cracks
07-11-20	37.809187	26.742978	Agios Nikolaos	road cracks
07-11-20	37.803605	26.724465	Kontakaiika north	road cracks
07-11-20	37.803592	26.724498	Kontakaiika north	road cracks
07-11-20	37.803588	26.724529	Kontakaiika north	road cracks
07-11-20	37.803583	26.724529	Kontakaiika north	road cracks
07-11-20	37.803582	26.724528	Kontakaiika north	road cracks
07-11-20	37.793980	26.670743	Potami	raised coastline
07-11-20	37.793825	26.670602	Potami	raised coastline
07-11-20	37.792297	26.668608	Potami	Raised beach
07-11-20	37.792455	26.668855	Potami	salt pans
07-11-20	37.792457	26.668863	Potami	raised beach
07-11-20	37.792517	26.668987	Potami	beach rock
07-11-20	37.798747	26.706262	Karlovasi	collapse
07-11-20	37.800574	26.709502	Karlovasi	collapse
07-11-20	37.800532	26.709530	Karlovasi	collapse
07-11-20	37.801080	26.708335	Karlovasi beach front	collapse
07-11-20	37.801087	26.708115	Karlovasi beach front	collapse
07-11-20	37.800833	26.708056	Karlovasi beach front	collapse
07-11-20	37.800385	26.705687	Karlovasi beach front	view to the east
07-11-20	37.800306	26.705436	Karlovasi beach front	collapse
07-11-20	37.800325	26.705346	Karlovasi beach front	collapse
07-11-20	37.773310	26.723260°	road to Kontaiika	collapse
07-11-20	37.767487	26.725427°	road to Kontaiika	wall damage (fence)
07-11-20	37.767429	26.725481	road to Kontaiika	wall damage (fence)
07-11-20	37.756800	26.738886	Kontaiika	collapse
08-11-20	37.753122	26.95935	Vathy new port	jetty damage
08-11-20	37.753122	26.95935	Vathy new port	jetty damage
08-11-20	37.753122	26.95935	Vathy new port	jetty damage
08-11-20	37.753122	26.95935	Vathy new port	jetty damage
08-11-20	37.756406	26.957641	Malagari	Building damage
08-11-20	37.756828	26.957874	Malagari	soil liquefaction
08-11-20	37.756853	26.958147	Malagari	road cracks
08-11-20	37.756729	26.958311	Malagari	tree line (submerged)
08-11-20	37.756804	26.957965	Malagari	soil liquefaction

08-11-20	37.756803	26.957965	Malagari	soil liquefaction
08-11-20	37.756827	26.957926	Malagari	soil liquefaction
08-11-20	37.756827	26.957924	Malagari	soil liquefaction
08-11-20	37.756729	26.958313	Malagari	tree line submerged
08-11-20	37.756729	26.958314	Malagari	tree line submerged
08-11-20	37.756728	26.958314	Malagari	tree line submerged
08-11-20	37.756727	26.958277	Malagari	ground offset
08-11-20	37.756727	26.958276	Malagari	ground offset
08-11-20	37.756729	26.958276	Malagari	ground offset
08-11-20	37.796431	26.678894	Karlovasi jetty	cracks
08-11-20	37.79643	26.678893	Karlovasi jetty	cracks
08-11-20	37.796433	26.67889	Karlovasi jetty	cracks
08-11-20	37.796432	26.678889	Karlovasi jetty	cracks
08-11-20	37.79643	26.678885	Karlovasi jetty	cracks
08-11-20	37.796432	26.678882	Karlovasi jetty	cracks
08-11-20	37.795377	26.678302	Karlovasi shipyard	tsunami upper limit
08-11-20	37.795377	26.678302	Karlovasi shipyard	tsunami upper limit
08-11-20	37.795154	26.678336	Karlovasi shipyard	tsunami extent limit

1052

1053

Fig. S1: Seismicity map (EMSC data) showing both magnitude and depth distribution of events.

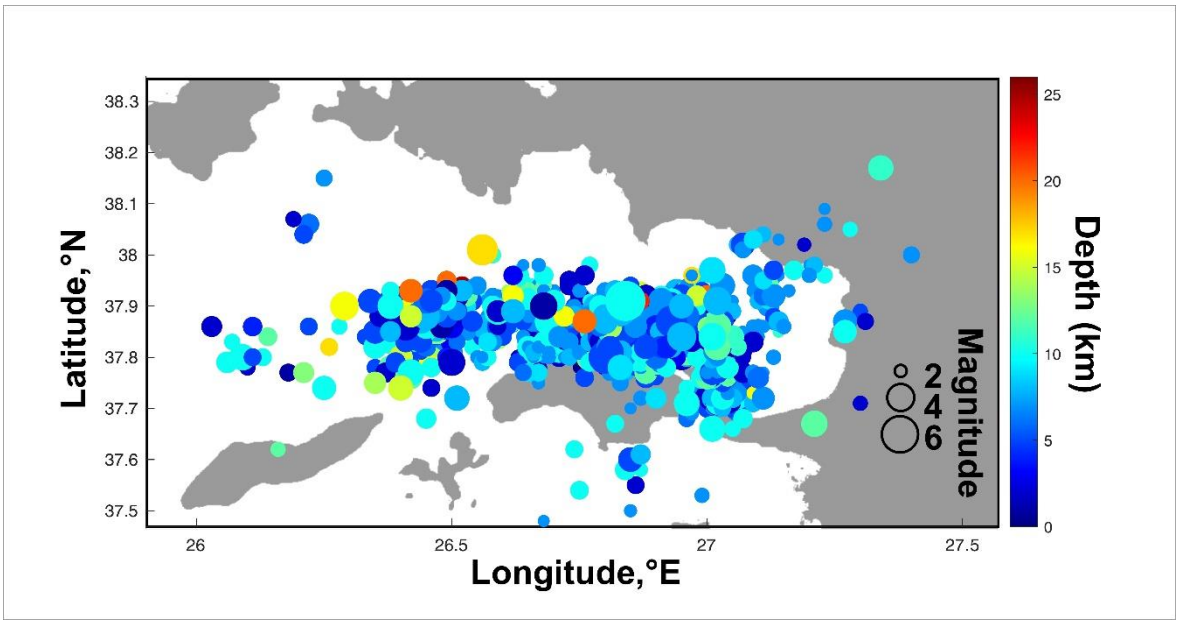

Fig. S2: The initial co-seismic differential interferograms (wrapped phase; cropped swath of ascending track 131; Ganas et al. 2020a) over Samos island, produced exploiting the Geohazards Exploitation Platform. Top panel shows the image pair 24 Oct. – 30 Oct., 2020. Bottom panel: 18 Oct. – 30 Oct., 2020. The fringes in the differential interferogram show a pattern that supports more the north-dipping plane as the density and the curvature of the fringes indicates. These data show that Samos moved towards the satellite in the LOS with the exception of a coastal strip from Agios Konstantinos to Kokkari that moved away. The interferograms are draped over Google Earth imagery.

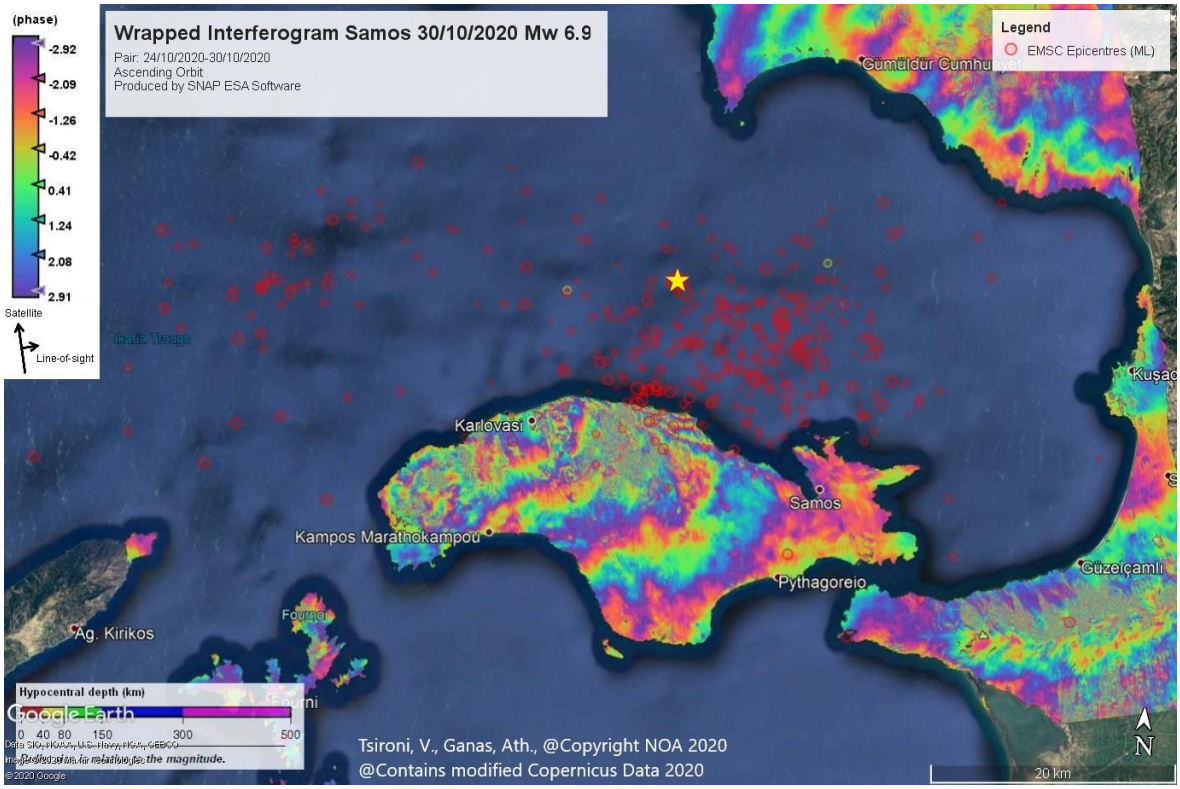

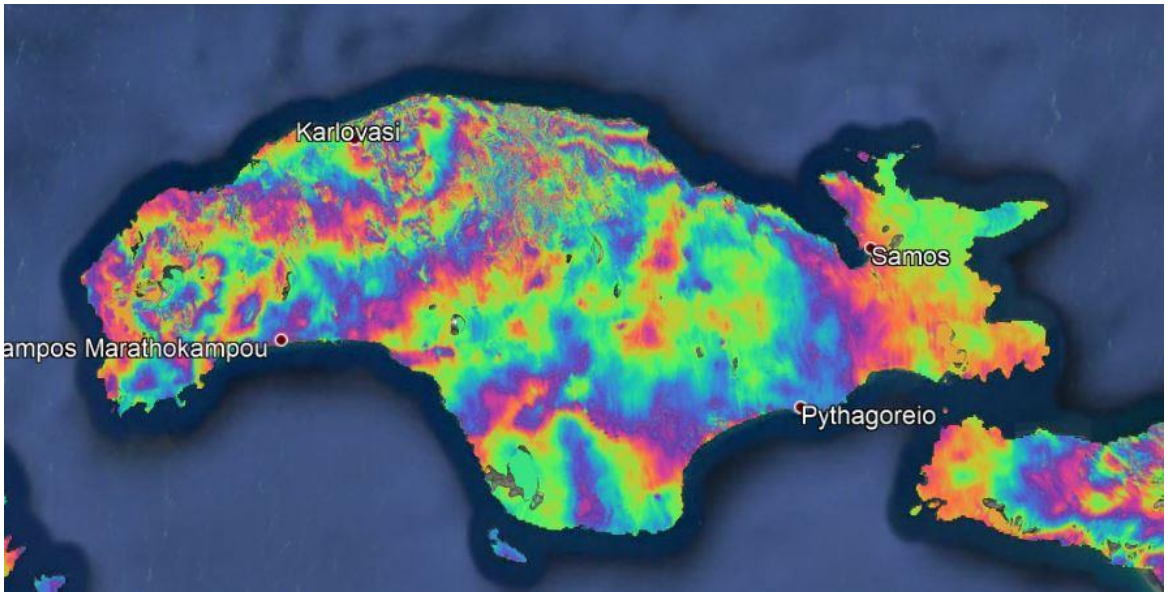

Fig. S3: (a) Best interferogram of Track 36 (D) spanning the dates 10 June – 11 November 2020, (b) the unwrapped one, (c) the average interferogram of the best four and (d) the unwrapped one.

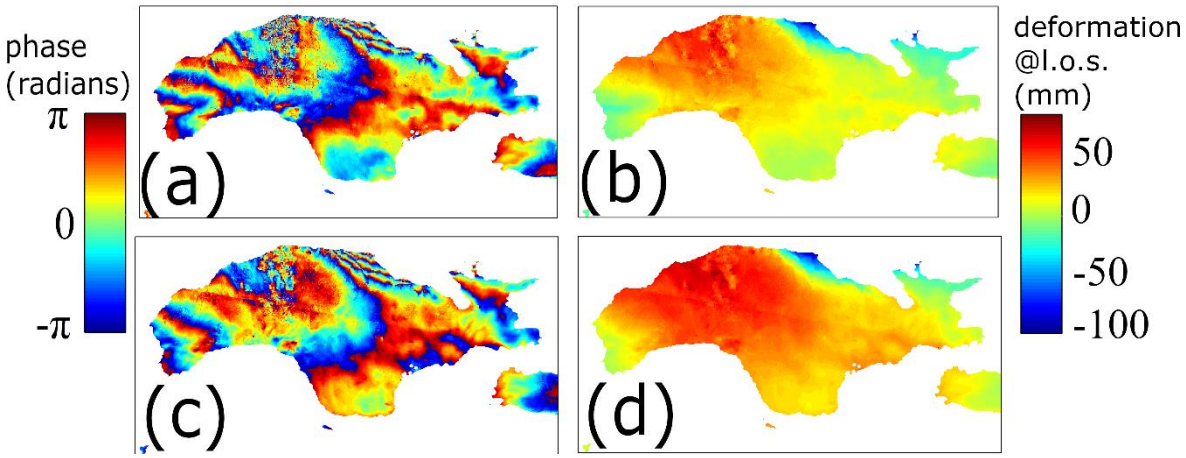

Fig. S4: Graphs with time series of GNSS coordinates of the SAMO (a) and 093A (b) GNSS station across the day of the earthquake (red vertical line in a).

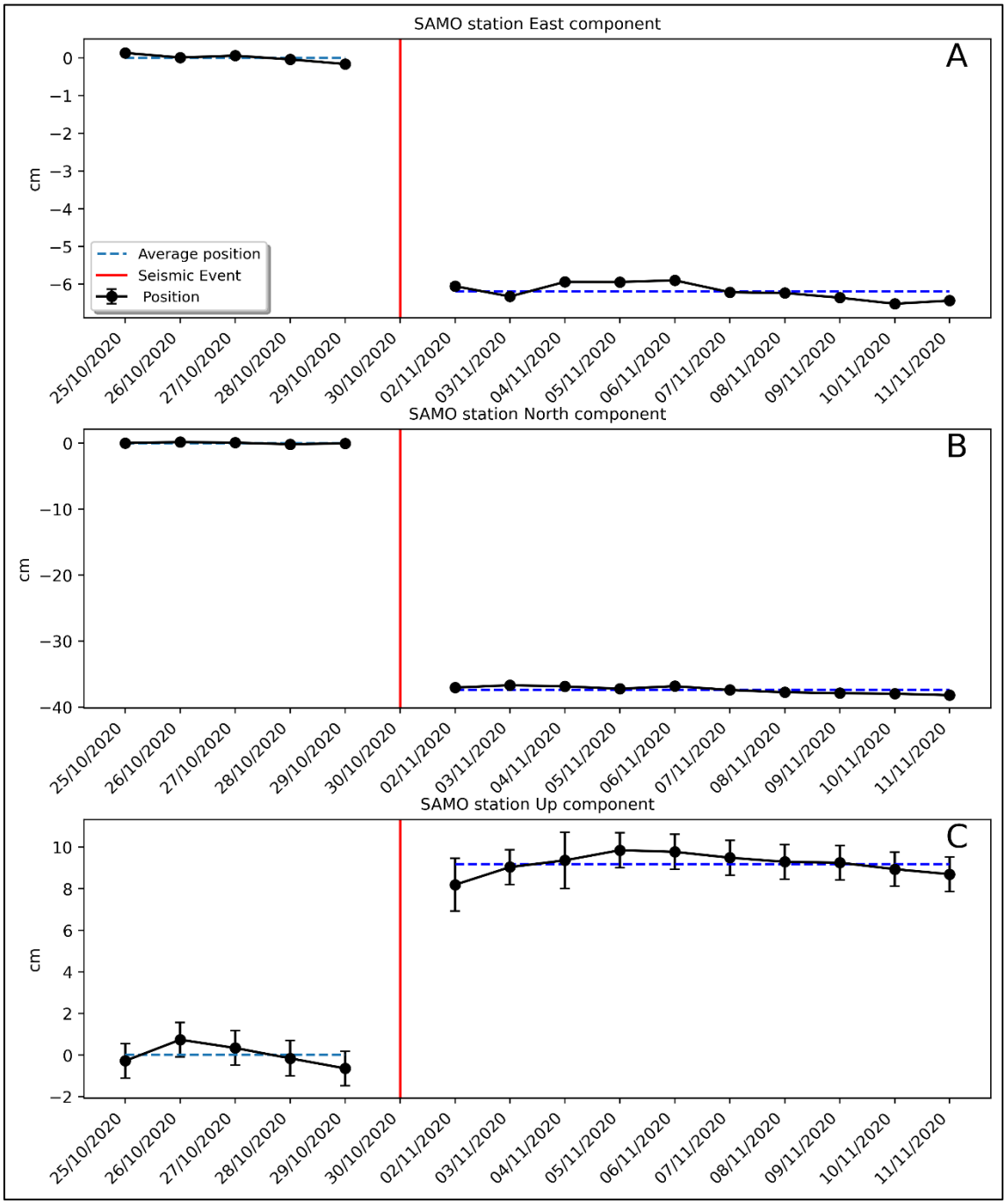

(a)

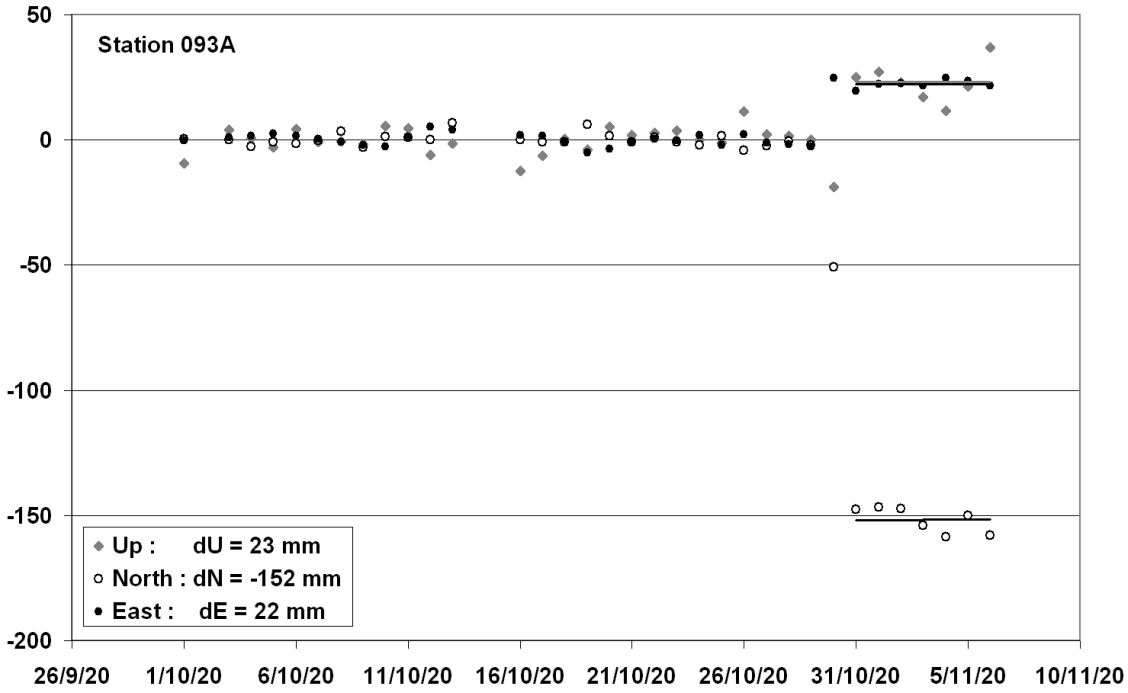
Station 093A
50
0
-50
-100
-150
-200
Up : dU = 23 mm
North : dN = -152 mm
East : dE = 22 mm
26/9/20
1/10/20
6/10/20
11/10/20
16/10/20
21/10/20
26/10/20
31/10/20
5/11/20
10/11/20

(b)

Fig. S5: Synthetic models of ground surface displacement using Okada-type dislocations in elastic half-space. The modeled dislocation (from Ganas et al. 2020a) has length/width of 36 km / 18 km, a finite slip of 1.82 m and a strike/dip/rake: 276°/37°/-90° (see GCMT and USGS moment tensor solutions from Table 1 on the main paper). Top panel) North-South displacement bottom panel) Up-Down displacement. Values are in m. Yellow star is the epicentre of the mainshock.

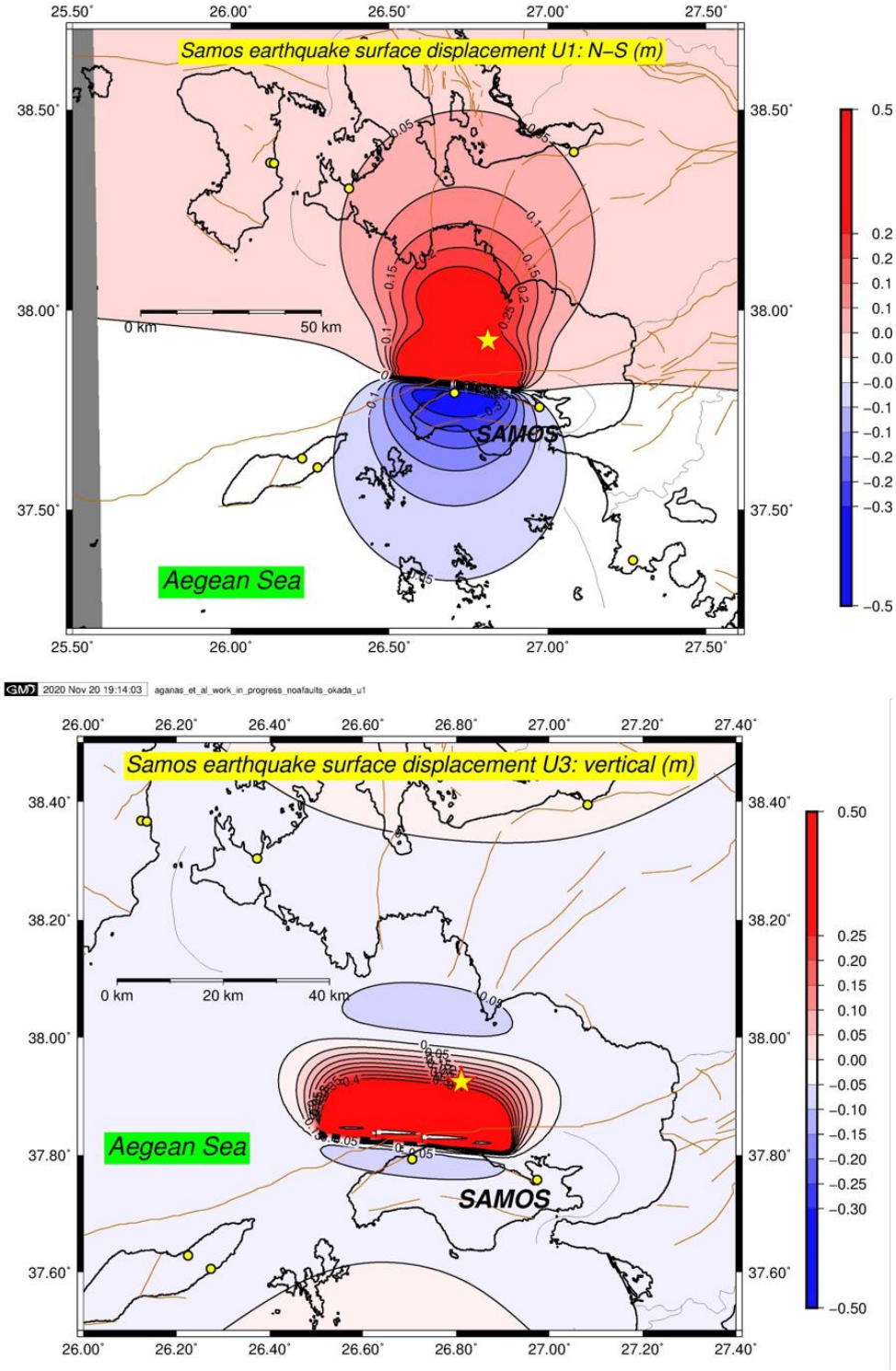

Fig. S6: Picked values in the two averaged interferogram (a) ascending track 29 and b) descending track 36/

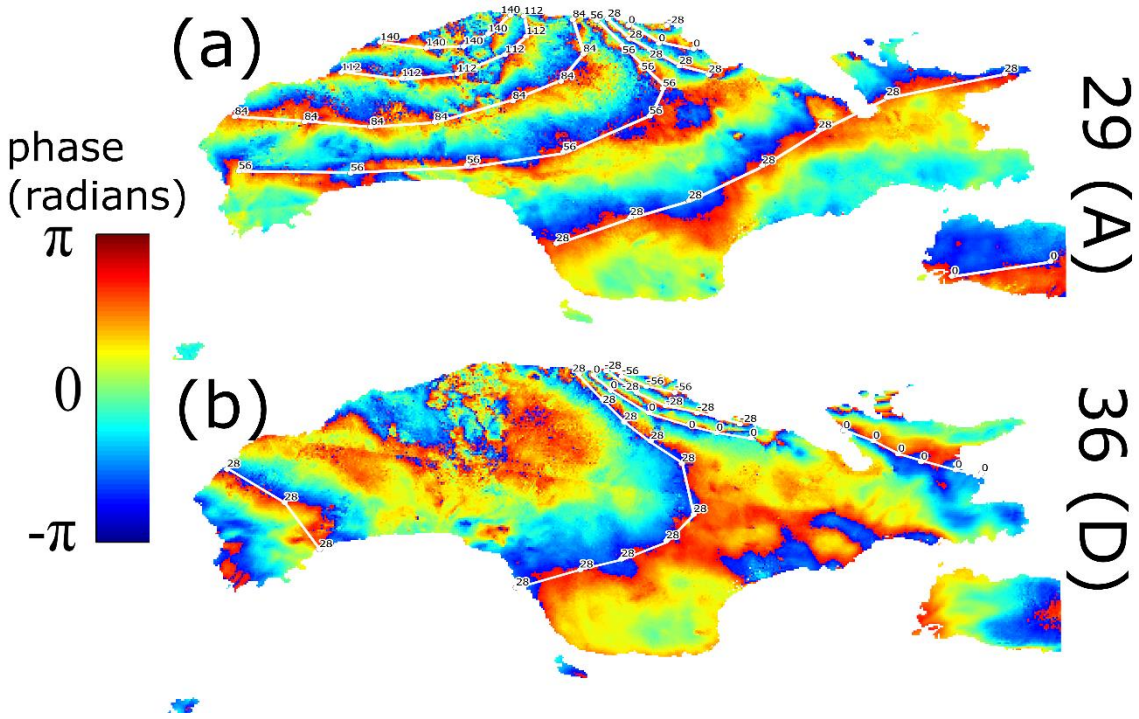

Fig. S7. Divergence diagrams of the set of inversions for a) fault azimuth (strike), b) depth to top-fault, c) length, d) width and e) normal slip.

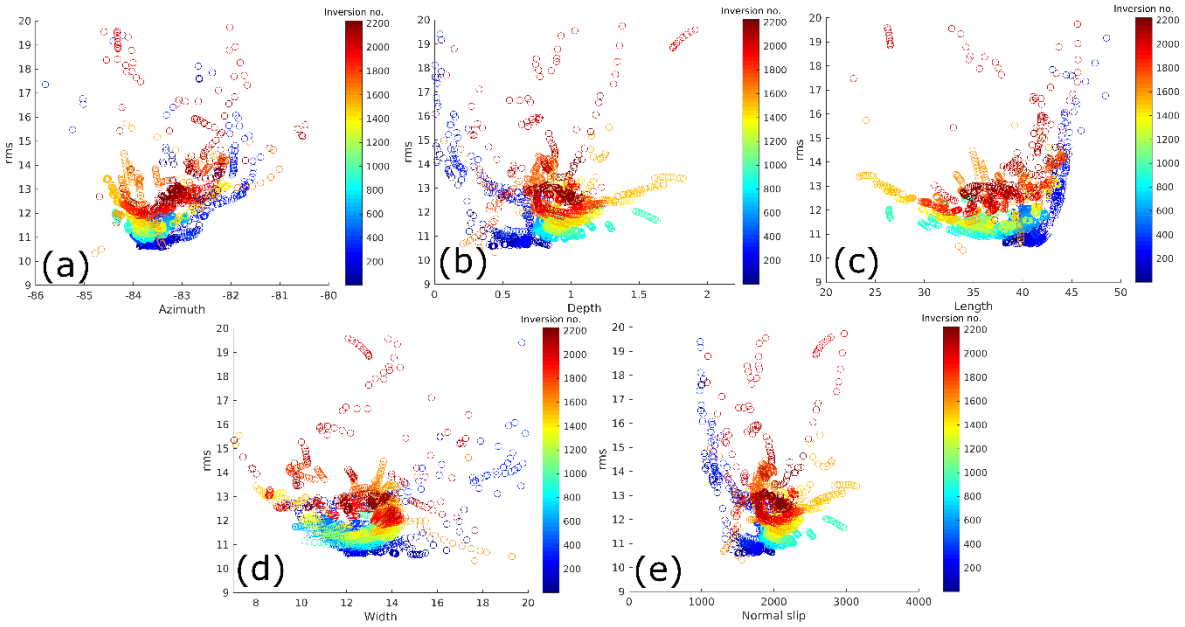

Fig. S8. Fault model from the InSAR data (synthetic model; descending orbit). The dip-direction is towards north. Arrows indicate GPS offset vectors (observed vs. predicted). The formation of the interferogram is at the notion of post-event minus pre-event image, thus phase decreasing towards satellite.

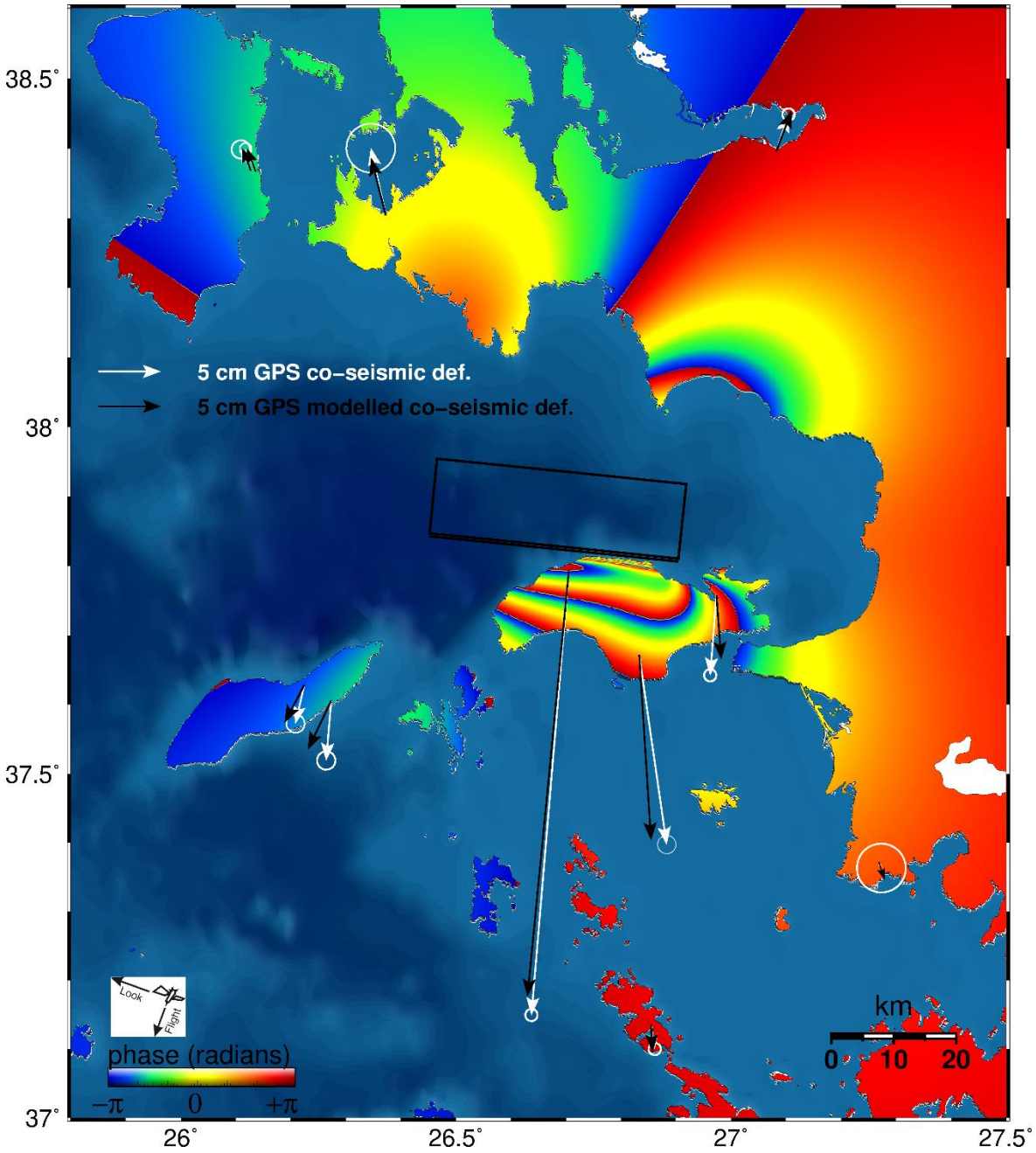

Fig. S9. Displacement profile onshore Samos showing a comparison of the InSAR observed values (LOS; track 29) versus the modelled values (see Fig. 8 of the main paper). The location of the profile is shown in Fig. 3.